The U-Nb-Al ternary system: experimental and simulated investigations of the phase equilibria and study of the crystal structure and electronic properties of the intermediate phases

Chantal Moussa, Alexandre Berche, Mathieu Pasturel, José Barbosa, Bertrand Stepnik, Sylvie Dubois, Olivier Tougait

Graphical abstract:

The phase relations in the ternary U-Nb-Al system were investigated by both experimental and modeling studies revealing a close agreement for the isothermal sections at 900K and 1200 K. The formation of the two ternary phases, UNb_2Al_{20} and $U_6Nb_4Al_{43}$ was determined according to the peritectic reactions: $NbAl_3 + UAl_3 + L \rightarrow U_6Nb_4Al_{43}$ and $NbAl_3 + U_6Nb_4Al_{43} + L \rightarrow UNb_2Al_{20}$. , occurring at 1262(5) K and at 1200(5) K respectively. Both compounds present typical cage like-structure. In the case of $U_6Nb_4Al_{43}$, adjacent cages allow the formation of U-U dimeric infinite zig-zag chains which may be responsible for its unusual magnetic features. At low temperature, a composite behavior is observed, showing both long-range and short-range orderings.

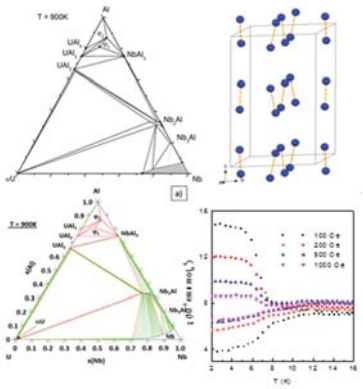

Titre:

The U-Nb-Al ternary system: experimental and simulated investigations of the phase equilibria and study of the crystal structure and electronic properties of the intermediate phases.

Auteurs:

Chantal Moussa[1], Alexandre Berche[1], Mathieu Pasturel[1], José Barbosa[1], Bertrand Stepnik[2], Sylvie Dubois[3] and Olivier Tougait[1,4]

Affiliation:

[1]*Institut des Sciences Chimiques de Rennes, UMR CNRS 6226, Université Rennes 1, Campus de Beaulieu, 35042 Rennes Cedex, France*

2 *AREVA/CERCA, 10 Rue Juliette Récamier, 69006 Lyon – France*

3 CEA/DEN/DEC, Cadarache, 13108 St. Paul Lez Durance, France.

[4]*Unité de Catalyse et de Chimie du Solide, UMR CNRS 8181, Université de Lille, 59695 Villeneuve d'Ascq, France*

Corresponding author : Olivier TOUGAIT, Unité de Catalyse et de Chimie du Solide, UMR CNRS 8181, Université de Lille, 59695 Villeneuve d'Ascq, France.

Email : tougait@univ-rennes1.fr

TEXT

Abstract: The phase relations in the ternary U-Nb-Al system were established for the whole concentration range for 900 K and 1200 K. They were derived from quenched samples annealed at 900 K for three months and at 1200 K for two months by using x-ray powder diffraction, scanning electron microscopy and energy dispersive spectroscopic analyses. The formation of the two ternary phases, UNb_2Al_{20} and $U_6Nb_4Al_{43}$ was confirmed. Both phases form by peritectic reaction, at 1200(5) K and at 1262(5) K for UNb_2Al_{20} and $U_6Nb_4Al_{43}$ respectively. Single-crystal structure refinements confirmed that UNb_2Al_{20} adopts the $CeCr_2Al_{20}$ type (cubic, $Fd\bar{3}m$) and that $U_6Nb_4Al_{43}$ crystallizes with the $Ho_6Mo_4Al_{43}$ type (hexagonal, *P6₃/mcm*). The isothermal sections are characterized by (i) the extended homogeneity ranges due to mutual exchange between U and Nb and between Nb and Al in the *bcc*-phases (γU and Nb), at 1200 K, and (ii) a substantial ternary extension with limits of about 6(1) to 10(1) at.% U at 900K and 1200K respectively, of the σ-phase (Nb_2Al, tetragonal). The modeling of these isothermal sections was carried out by the Calphad method. The liquidus projection and the invariant reactions along with their corresponding temperatures were calculated using our optimized database. The electronic properties of both intermediate compounds were measured by means of *dc*-susceptibility, specific heat and resistivity measurements in the temperature range 2-300K, revealing for UNb_2Al_{20} an enhanced Pauli paramagnet and complex magnetic features for $U_6Nb_4Al_{43}$ at low temperature. For the latter compound a composite behavior involving long-and short-range orderings, resulting from intra and inter U dimeric chains along the c-axis is suspected below 12 K.

Keywords : Keywords : A-actinide alloys and compounds; B-rapid-solidification, quenching; C-electronic properties; C-heavy fermions; D-thermodynamic modeling; D-X-ray diffraction.

1. Introduction:

The U-Nb system has been widely studied due to remarkable physical properties and transformation mechanisms (diffusion and diffusion-less ones) of its alloys. Depending on both the cooling rates and the Nb-content, the various metallurgical states obtained exhibit rather opposite mechanical properties and corrosion behaviors [1-6]. Slowly cooled samples with low Nb-content display weak corrosion resistance and mechanical properties associated to a two-phase microstructure composed of grains of αU based phase (denoted α' and α'', orthorhombic and monoclinic) and of distorted γU based phase (denoted γ^0, tetragonal). Conversely, samples with higher Nb content of about 20 at. %, quenched with high cooling rates, exhibit a homogenized microstructure composed of grains of the cubic γ(U,Nb) phase which show improved corrosion resistance and high ductility. Considering that this second type of alloys still possesses a high U density and that Nb has a low neutron absorption cross-section, these γ(U,Nb) alloys are of interest for nuclear applications, mainly as nuclear metallic fuel.

Indeed, within the framework of the Reduced Enrichment Research and Test Reactor (RERTR) international program which focusses on the development of a U-dense fissile material stable under severe irradiation conditions, the U-Nb based alloys can be seen to have some interest for Al-dispersion fuel-plates. In these dispersed fuels, the fissile material is embedded in an Al-matrix and then cladded by Al foils in order to form a thin fuel plate. In this respect, the phase equilibria and compatibility within the ternary U-Nb-Al system can provide valuable information for the fabrication process and the in-pile behavior. To reach this goal, the assessment of the ternary U-Nb-Al phase diagram will establish the formation and thermal stability of the intermediate phases. Up to now, no ternary phase relation is reported for the U-Nb-Al ternary system.

The present article summarizes our study of the U-Nb-Al ternary system which is based on a combined approach to the experimental assessment of the isothermal sections at 900 K and 1200 K with their thermodynamic modeling by the CALPHAD method. The assessed thermodynamic database was further used to calculate the liquidus projection and the invariant reactions along with their temperature. The two intermediate phases, UNb_2Al_{20} and $U_6Nb_4Al_{43}$, which were recognized to crystallize with the $CeCr_2Al_{20}$ and $Ho_6Mo_4Al_{43}$ structure-types, respectively [7, 8], are typical cage-like compounds. In such a structure,

where magnetic ions are located at the center of the cages, various interesting electronic phenomena are observed, like unconventional superconductivity, as identified in UBe_{13} [9] more than thirty years ago. Therefore, these two U-Nb-Al ternary compounds were further characterized. Their crystal structure was refined from single crystal x-ray diffraction data, their formation mode was assessed and some of their electronic properties were measured by means of *dc*-magnetic susceptibility, electrical resistivity and specific heat experiments.

2. Experimental section:

The polycrystalline samples have been prepared by melting the elemental components in an arc-furnace. The samples, placed in alumina crucibles, were introduced and sealed in evacuated silica tubes under a residual atmosphere of argon. The reaction tubes were annealed at 1200 K for two months or at 900 K for three months and then quenched to room temperature. Alternative heat-treatments were carried out on selected samples, in a high-frequency furnace under low Ar-pressure. The arc-melted ingots were placed into a copper cold-crucible for annealing in the temperature range 1473-1673 K, with dwell periods of about 6 hours.

Each bulk sample was analyzed by powder X-Ray Diffraction (XRD) collected at room temperature using a Bruker AXS D8 Advance diffractometer *(*θ*-2*θ Bragg-Brentano geometry, monochromatized Cu $K\alpha_1$ radiation, λ=1.5406 Å), equipped with a LynxEye fast detector. The experimental diffraction patterns were compared to those calculated from known structure types using the PowderCell software [10]. Besides the profile parameters of the x-ray powder patterns, lattice and atomic parameters were refined with the help of the Le Bail and Rietveld methods, respectively, implemented in the FullProf suite [11].

The microstructure of the samples was examined on polished surfaces using a Jeol JSM 7100F Scanning Electron Microscope (SEM) equipped with a Silicon Drift Detector (SDD) - X-Max 50 from Oxford Instrument employed for the elemental analysis of the various phases. Elemental compositions obtained by Energy Dispersive Spectroscopy (EDS), were corrected by using U, Nb and Al metals and binary compounds with point composition or minute homogeneity range, such as UAl_3, UAl_2 and $NbAl_3$, as external standards to derive semi-quantitative data. The presented figures were obtained by averaging the values of at least

three areas on the same phase in different regions of the samples. An estimated deviation from the mean value is about 1.0 at.% (± 0.5 at. % absolute error).

Differential Thermal Analysis (DTA) was performed on a Setaram LabSys 1600 apparatus, calibrated using the phase transitions and melting temperatures of different pure metals (Al, Cu, Fe). The measurements, carried out in alumina crucibles, were performed up/down to/from 1873 K at a heating/cooling rate of 5 K min^{-1}, under a 5 N purity argon flow.

Small single crystals suitable for crystal structure determination were picked up from the heat-treated samples. The diffraction intensities were collected at room temperature on a Nonius Kappa CCD four-circle diffractometer working with Mo Kα radiation (λ = 0.71073 Å). The integration and reduction of redundant reflections of the different data sets as well as the cell refinements were performed using the SADABS software [12]. Structural models were determined by direct methods using SIR-97 [13]. All the structure refinements and Fourier syntheses were made with the help of SHELXL-13 [14]. The atomic positions have been standardized using STRUCTURE TIDY [15].

The magnetic properties were studied in temperature range 2-300 K and in magnetic fields up to 5 T using Quantum Design MPMS SQUID magnetometer. The specific heat and electrical resistivity were measured at temperatures 2-300 K using a Quantum Design PPMS physical measurement platform.

The thermodynamic modeling using the calculation of phase diagrams by the CALPHAD method was carried out with the Thermo-Calc software [16].

3. Literature data

The structural as well as some thermodynamic data of the unary and binary phases relevant to the present study were mostly accepted from the critical assessment of the binary alloy phase diagrams by Massalski [17] with some recent modifications.

The phase equilibria in the binary U-Al system are described in detail by Kassner *et al*. [18]. The phase diagram comprises three intermediate phases, UAl_2, UAl_3 and UAl_4. UAl_2 is characterized by a congruent melting point at 1893 K, UAl_3 and UAl_4 form by peritectic reactions at 1623 K and at 1005 K, respectively. The main conflict with more recent results

concerns the latter compound, which forms as a stoichiometric compound without constitutional defect in the U sublattice, ruling out the existence of two polymorphic forms due to an order (α form) and a disorder (β form) of the vacancies [19]. The most recent thermodynamic assessment of the U-Al binary system [20] took into consideration these changes. In the present work, this latest description is taken into account for the thermodynamic modeling of the U-Nb-Al system.

The accepted depiction of the U-Nb system arises from the compilation of Koike *et al*. [21]. The phase diagram is characterized by a complete solid solution between γU and Nb above 1250 K. Below this temperature, the γ(U,Nb) phase goes through a miscibility gap, γU + Nb, for samples containing less than 77 at. % Nb,. The phase separation extends from 13.3 to 70 at. % Nb at 920 K, the temperature below which the γU phase undergoes a peritectoid decomposition. No stable intermediate phase is reported to form, but a metastable one, denoted δ-phase, was observed in diffusion couple experiments [22]. This phase is located on the Nb-rich side of the miscibility gap. At 873 K, its composition is about 78 at. % Nb. The thermodynamic assessment of the U-Nb system is due to Liu et al. [23].

The Nb-Al system has been extensively studied, revealing a terminal solid solution based on Nb and three intermediate phases, Nb_3Al (δ-phase), Nb_2Al (σ-phase) and $NbAl_3$ (ε-phase). Jorda et al. [24] reviewed the available literature data on phase relations, the solubility ranges and the crystallographic data, and completed the description of the phase diagram by an experimental work on the Nb-rich part. The system was firstly optimized by Kaufman [25] and Servant & Ansara [26] and more recently by Zhu et al. [27], Witusiewicz et al. [28] and He et al. [29]. The main differences between these two sets of models lie (*i*) in the comprehension of the invariant equilibrium in the Al-rich side and (*ii*) the description of Nb_2Al (σ–phase). The precise nature of the reaction was experimentally determined as peritectic [27, 28] and thus included in the recent assessments. The sublattice model $(Al,Nb)_{16}Nb_4(Al,Nb)_{10}$ which is in better agreement with the crystallographic data, is recommended for use in ternary systems. The latest assessment [29] has been selected for our thermodynamic modeling of the U-Nb-Al ternary system.

Table 1 summarizes the main crystallographic data and some miscibilities for the unary and binary phases bounding the U-Nb-Al system. It should be noted that βU and Nb_2Al have the same crystal structure.

Please insert here Table 1

Two U-Nb-Al ternary phases are reported in the literature: UNb_2Al_{20} [6] and $U_6Nb_4Al_{43}$ [7]. They belong to two large families of isostructural compounds adopting the cubic $CeCr_2Al_{20}$-type and the hexagonal $Ho_6Mo_4Al_{43}$-type, respectively. They were obtained by annealing arc-melted ingots with the stoichiometric composition at 1073 K for three weeks.

4. Results and discussion.

4.1 Isothermal sections of the U-Nb-Al ternary system.

4.1.1 Description of the experimental phase relations

The experimental phase equilibria of the U-Nb-Al phase diagram at 900 K and 1200 K are depicted in Figures 1 and 2 respectively. The thick solid lines define the boundaries between the various fields. The white, dashed line-filled and grey areas correspond to three-phase, two-phase and single phase fields respectively. They have been constructed from the combined results of the semi-quantitative and powder x-ray diffraction analyses of samples covering the whole concentration range which were heat-treated for three months and two months, for the isotherms at 900 K and 1200 K, respectively, before being water-quenched. Selected samples defining two-phase fields and three-phase fields are compiled in Table 2 and 3, for both respective isotherms. The description of the isothermal sections is divided into three parts corresponding to (*i*) the solubility ranges in the unary and binary phases, (*ii*) the Al-poor and (*iii*) the Al-rich regions with a border at 75 at. % Al.

Please insert here Figure 1 and Figure 2

Please insert here Table 2 and Table 3

4.1.2 Solubilities in the unary and binary phases at 900 K and 1200 K.

Most of the binary phases involved in the U-Nb-Al system were already observed from arc-melted samples, hindering a proper evaluation of the solubility ranges for the isothermal sections. Therefore, to appraise the effects of the heat-treatments on the homogeneity ranges, and especially to evaluate the solubility limits in the vicinity of the Nb_2Al phase, SEM-EDS analyses were compared for selected samples (*i*) in the as-cast state, (*ii*) heat-treated in a high-frequency furnace at 1523 K for 6 hours and (*iii*) annealed at 1200 K for two months. Significant effects on the growth of the grain size and the chemical homogenization were

observed for annealing times of two months at 1200 K. As an example the upper Al-content in the Nb_2Al-phase was found to be 42 at. % Al in the as-cast sample, whereas it is only 36 at. % Al in the sample heat-treated at 1200 K. (Table 4). Despite prolonged annealings of three months at 900 K for the bulk samples, the grain size for the Nb-rich phases remains quite small (few μm), resulting in enlarged errors of the measured homogeneity ranges.

No solubility above 1 at. % of the other elements was measured in Al at 900 K, and its liquid extension at 1200 K was not evaluated experimentally. The solubilities of both Al and U in the Nb solid solution are compared to the values deduced from the previous investigations [21, 24], with maximum solubilities estimated at about 23 at. % U and 7 at. % Al at 900 K and at about 38 at. % U and 8 at. % Al at 1200 K. The solubility of Al and Nb in the allotropic α-forms of U metal was found null at 900 K, whereas they amount to 2.5 at. % Al and 40 at. % Nb at 1200 K. These homogeneity ranges compare well with the reported values of the literature (Table 1).

As expected, the following binary phases were found stable at 900 K and/or at 1200 K: UAl_2, UAl_3, UAl_4, $NbAl_3$, Nb_2Al and Nb_3Al. The solubility of Nb in UAl_4 and UAl_3 was found null at the investigated temperatures (UAl_4 is only stable at 900 K), whereas a minute solubility was detected in UAl_2. it amounts to 1 and 2.5 at. % Nb at 900 K and 1200 K respectively. A substitution mechanism involving an Al/Nb exchange is suggested by the EDS analyses.

Please insert here Table 4

Our experimental solubility ranges in the binary Nb-Al system at 1200 K are presented in Table 4. They are compared to the experimental values of Jorda *et al*. [21] and the calculated ones of Zhu *et al*. [27], Witusiewicz *et al*. [28] and He et al. [29]. Our values, deduced from EDS-analyses are consistent with the reported elemental compositions for $NbAl_3$ and Nb_3Al, but show some discrepancies with most of the literature data for the Nb_2Al phase. The observed shift to higher Al-content is found to be in reasonable agreement with the values of the recent assessment of He *et al*. [29] only, justifying the selection of the corresponding database for the thermodynamic assessment of the U-Nb-Al ternary system. Regarding the U solubility in the Nb-Al binary phases, no solubility was found in $NbAl_3$ at both investigated temperatures, whereas a minute solubility of about 1 at. % U was assessed for Nb_3Al at 900 K and 1200 K. Based on EDS analyses the substitution of Nb by U is suspected. In contrast to $NbAl_3$ and Nb_3Al, Nb_2Al has a high U solubility of about 6(1) and 10(1) at. % U at 900 K and

1200 K, respectively. Given that the shape of the ternary extension of the Nb_2Al phase was not easy to determine by EDS analyses owing to a possible double substitution mechanism, single crystal x-ray diffraction experiments were carried out to ascertain the occupancy rate of the crystallographic sites. The diffracted intensities were collected at room temperature on a fragment of a crushed ingot with an initial composition of 10U-60Nb-30Al heat-treated at 1473 K for 6 hours in a high frequency furnace. The refinements were carried out in the tetragonal space group *$P4_2/mnm$* (no. 136) with an initial structural model based on the Nb_2Al-phase [37]. The distribution of atoms on the Wyckoff sites is three Nb on *8j*, *8i* and *4g* and two Al on *8i* and *2a*. Refinements with this initial model displayed some deficiency of the electronic density in the vicinity of the *4g* site occupied by the Nb(1) atom, suggesting that this position is also occupied by U. In subsequent refinements, the occupancy level of the *4g* site converges to an U occupancy around 1/5. Additional cycles of refinement, performed with Nb/Al mixed occupancy on the Al sites located on the *8i* and *2a* sites, yielded low residual electron densities in the Fourier map. The chemical formula deduced from the single crystal refinement is $U_{0.08}Nb_{1.95}Al_{0.97}$ yielding the atomic ratio 3U-65Nb-32Al which compares well the limit of the three-phase field for a sample with the initial composition 10U-60Nb-30Al (see below the 4.1.3 sub-section). Our single crystal diffraction experiments confirm the occurrence of two substitution mechanisms of Nb in *4g* site by U, and of Al in *8i* and *2a* by Nb. Therefore the formula of the ternary extension of σ-phase is best represented by $U_xNb_{2-x+y}Al_{1-y}$. The deviation from the ideal Nb_2Al stoichiometry can be regarded as a general feature of the σ-phase [39]. Extending this model to full U/Nb substitution on the *4g* site would lead to a chemical formula of $U_{0.4}Nb_{1.6}Al_1$ giving the atomic ratio 13.3U-53.3Nb-33.3Al as the limit of the ternary extension of the Nb_2Al phase in the U-Nb-Al ternary system. This value is in a reasonable agreement with the U solubility of 12.5 at. % U, measured for as-cast samples.

The relevant data concerning the single crystal x-ray diffraction data collection done for $U_{0.08}Nb_{1.95}Al_{0.97}$ are gathered in Table 5. The atomic positional and thermal displacement parameters are listed in Table 6.

Please insert here Table 5 and Table 6.

Given the metallic radii of U, Nb and Al (r(U) = 1.53 Å, r(Nb) = 1.47 Å and r(Al) = 1.43 Å), the substitution of Nb by U is expected to be accompanied by an increase of the unit-cell

volume, whereas the substitution of Nb by Al will result in an opposite effect. Refinements of the lattice parameters using the Le Bail method from powder XRD data collected on samples annealed at 1200 K confirm this hypothesis (Table 7). The elemental composition corresponds to the average atomic ratio deduced from the EDS analyses. The U substitution introduces anisotropic effects between the basal plane showing a decrease of the *a*-parameter and the orthogonal plane showing an increase of the *c*-parameter, compared to the non-substituted binary phase. The unit-cell volume, the lattice parameters and the elemental composition deduced from the single crystal refinement fit quite well with this trend, suggesting that the U substitution for Nb follows a mechanism with a mixed occupancy of the *4g* site within the ternary extension of the present σ-phase.

Please insert here Table 7.

4.1.3. The Al-poor region (below 75 at. % Al).

The phase equilibria in this area of the phase diagram are dominated by the relations involving the $U_xNb_{2-x+y}Al_{1-y}$ -phase (σ-phase). Its extension into the ternary phase diagram significantly progresses with the increase of the temperature as described above. It is involved in five two-phase fields and four three-phase fields which evolve with its extension into the ternary triangle within the investigated temperature range. It results in the stabilization of the two-phase fields involving $U_xNb_{2-x+y}Al_{1-y}$, as illustrated by the shrinkage of the two-phase field between Nb_3Al and Nb between 900 and 1200 K. This suggests that the thermodynamic stability of Nb_2Al, mainly its entropic component, increases with temperature. At 1200 K, $U_xNb_{2-x+y}Al_{1-y}$ develops a large two-phase field domain with γ(U,Nb) covering the entire *bcc* solid solution (up to 40 at. % Nb), causing $UAl_{2-x}Nb_x$ to be in equilibrium with γU only. EDS analyses of quenched samples show an U-rich phase with Nb content of less than 2 at. %. The corresponding XRD patterns were found compatible with the α-form of U (or α' and α '' distorted forms) in agreement with the previous works [1, 2].

4.1.4. Phase relations in the Al-rich region (above 75 at % Al).

At 900 K, the Al-rich part of the phase diagram is dominated by the ternary phases UNb_2Al_{20} (labelled φ_2) and $U_6Nb_4Al_{43}$ (labelled φ_1), defining six three-phase fields. The EDS analyses indicate that they both crystallize as line-compounds, but with a very small

deviation from the ideal composition for UNb_2Al_{20}. Such a shift of composition was already observed for several members of this family of compounds adopting the $CeCr_2Al_{20}$-type (cubic, $Fd\bar{3}m$, n°227). It results (*i*) from a substitution of the transition metal by some Al at the *16d* Wyckoff position [6, 40] or (*ii*) from vacancy of Al on the *16c* Wyckoff site [41]. Similarly, the $Ho_6Mo_4Al_{43}$ structure-type (hexagonal, *P6₃/mcm*), adopted by $U_6Nb_4Al_{43}$ is also known to display some homogeneity ranges. In this case also a transition metal / aluminium substitution is observed. It occurs mainly on the *8h* Wyckoff sites [40, 42]. The possible off-stoichiometry of UNb_2Al_{20} and $U_6Nb_4Al_{43}$ was checked by single crystal XRD. Single crystals were isolated from crushed ingots having the ideal stoichiometry of UNb_2Al_{20} and $U_6Nb_4Al_{43}$, which were heat-treated at 1173 K for 10 days. The conditions for crystal data collection are gathered in Table 5.

For UNb_2Al_{20}, the refinements of the occupancy parameters were performed for the 5 non-equivalent positions, resulting in a small divergence from the full occupancy, at the *16d* Wyckoff position only. In subsequent refinements, this position was considered with a Nb/Al mixed-occupancy. The chemical formula thus deduced is $UNb_{1.9}Al_{20.1}$, indicating a very small deviation which was expected from the EDS results. For $U_6Nb_4Al_{43}$, refinements of the occupation parameters indicated the full occupancy of the crystallographic positions with the atomic distribution expected from the structural type. The chemical formula deduced from the structural refinement fits well with the EDS analysis. The refined atomic positions and equivalent displacement parameters are given in Table 8 and Table 9 for UNb_2Al_{20} and $U_6Nb_4Al_{43}$, respectively.

Please insert here Table 8 and Table 9.

The isothermal section at 1200 K, between 75 and 100 at. % Al shows three-phase field domains only, distributed by the $U_6Nb_4Al_{43}$ ternary phase. Along with the expected decomposition of UAl_4, the destabilisation of UNb_2Al_{20} is also observed for this high temperature section. To more precisely determine the thermal stability of both UNb_2Al_{20} and $U_6Nb_4Al_{43}$ compounds, DTA measurements were carried out in the temperature range 400 to 1400 K on pure polycrystalline samples. Two endothermic peaks were observed upon heating, indicating decomposition temperatures at 1200(5)K and 1262(5)K for UNb_2Al_{20} (φ_1) and $U_6Nb_4Al_{43}$ (φ_2) respectively. In agreement with the XRD and SEM-EDS analyses of Al-rich samples in the as-cast and heat-treated states the following peritectic reactions are considered: (*i*) $NbAl_3 + UAl_3 + L \rightarrow U_6Nb_4Al_{43}$ and (*ii*) $NbAl_3 + U_6Nb_4Al_{43} + L \rightarrow UNb_2Al_{20}$. One

can notice the absence of φ_1 of the isothermal section at 1200 K, which is fully in agreement with the decomposition temperature deduced from the DTA measurements.

4.2. Thermodynamic assessment of the U-Nb-Al ternary system

4.2.1 Model of the phases in the Calphad method

The liquid phase of each binary system is described with one sub-lattice, with the (Al, Nb, U)$_1$ model. The solid solutions based on the allomorphic forms of the elements are expressed as a substitution model using the Redlich-Kister polynomial function. The description of the Gibbs energy (^0G_i) is given for each phase by:

$$^0G_i = \sum_{i=A,B,C} x_i \, ^0H_i^{SER}(298.15K) = {}^{ref}G + {}^{id}G + {}^{XS}G \qquad \text{(I)}$$

where x_i is the molar fraction of the *i* element, H_i^{SER} represents the enthalpy of the pure element i and the reference term is:

$$^{ref}G = \sum_{i=A,B,C} x_i (^0G_i(T) - {}^0H_i^{SER}(298.15K)$$

where ^0G_i is the standard Gibbs energy of element i, ^0H_i is the standard enthalpy of the pure element i and the ideal term is:

$$^{id}G = RT \sum_{i=A,B,C} x_i \ln(x_i)$$

R is the universal gas constant and the excess term is:

$$^{XS}G = x_A x_B x_c \sum_n x_i \, ^nL_{A,B,C}(x_A - x_B - x_c)^n$$

with the interaction parameter is defined as $^nL_{A,B,C} = a + bT$.

In line with the recent work for the three intermediate phases of the Nb-Al system,[29] some homogeneity ranges were taken into consideration. The choice of this database was guided by a better agreement with our experimental observations of the solubility range of the Nb_2Al phase compared to the previous thermodynamic assessments [27, 28]. The model for the Gibbs energy functions has been developed according to crystallographic considerations. The sublattice formula of $(Al,Nb)_{0.25}(Al,Nb)_{0.75}$ was retained for the $NbAl_3$ phase whereas $(Al,Nb)_{0.25}(Nb)_{0.75}$ was used for the Nb_3Al phase. For the σ-phase (Nb_2Al), the commonly accepted sublattice model $(Nb,Al)_{16}(Nb)_4(Al,Nb)_{10}$, which corresponds to the

atomic occupations of crystallographic sites (8i,8j)(4g)(2a,8i) of the *$P4_2/mnm$* space group, was retained in our assessment as $(Al,Nb)_{0.534}(Nb)_{0.133}(Al,Nb)_{0.333}$.

The other phases, both the U-Al binaries and U-Nb-Al ternaries, are treated as line compounds. Since no experimental high temperature heat- capacity was reported, the Gibbs energy is assigned to the stable states of the constituting elements according to the Kopp-Neumann rule:

$$G(x_A A x_B B x_C C) = x_A G_A^{SER} + x_B G_B^{SER} + x_C G_C^{SER} + a + bT$$

4.2.2 Thermodynamic assessment

The weak solubility of Nb in UAl_2 and of U in Nb_3Al has been evaluated with Nb/Al and U/Nb substitution mechanisms respectively as experimentally suggested by EDS analyses. The model of the U solubility in Nb_2Al (σ-phase) was expressed in accordance with the crystallographic investigations presented in sub-section 4.1.2 showing that U occupies the 4*g* Wyckoff site as a mixed position with Nb leading to $(Al,Nb)_{0.534}(Nb,U)_{0.133}(Al,Nb)_{0.333}$.

The ternary compounds UNb_2Al_{20} and $U_6Nb_4Al_{43}$ were treated as stoichiometric phases, despite the low deviation of the atomic occupancy deduced from the structural refinement of UNb_2Al_{20} (table 8). Their enthalpy of formation was adjusted to match the phase equilibria in the Al-rich part. Entropic parameters have been refined to be consistent with the decomposition temperature measured by DTA (1262(5) K and 1200(5) K for $U_6Nb_4Al_{43}$ and UNb_2Al_{20}, respectively).

The assessed parameters, which are gathered in Table 10, accurately reproduce the experimental composition limits and the equilibrium relations of the U-Nb-Al system at 900 K (Fig. 3) and 1200 K (Fig. 4). For both temperatures, the main variations with experimental measurements consist in the composition of the *bcc*-phases (Nb and γU) in equilibrium with the ternary extension of Nb_2Al (σ-phase): the calculated compositions are too rich in Nb. This phenomenon can be ascribed to the interaction parameters in the binary U-Nb system. Addition to our database of ternary interaction parameters was not able to correct this overestimation of the Nb-content of the *bcc*-phases as the limits of the three-phase fields, $\gamma(U,Nb)$-$U_xNb_{2-x}Al_{1-y}$-$UAl_{2-x}Nb_x$ and (Nb,U)-$Nb_{3-x}U_xAl$-$U_xNb_{2-x}Al_{1-y}$. As a consequence, the thermodynamic description of the U-Nb system would have to be

improved, but prior to that, other U-Nb-X ternary systems would have to be investigated to confirm this phenomenon.

Please insert here Table 10

Please insert here Figure 3 and Figure 4.

4.2.3 The U-Nb-Al ternary system at high temperature

The calculated liquidus projection is depicted in Fig. 5 along with the primary solidification phases. The calculated invariant reactions involving the liquid with their temperature are listed in Table 11. Even if these results were obtained without any ternary interaction parameters, the predicted phase formations from the liquid compare well with the experimental phase identification carried out on as-cast samples, showing the presence of binary and unary phases only.

Please insert here Figure 5.

Please insert here Table 11.

4.3. Electronic properties of UNb_2Al_{20} and $U_6Nb_4Al_{43}$.

The electronic properties of UNb_2Al_{20} and $U_6Nb_4Al_{43}$ were measured on polycrystalline samples. XRD and SEM-EDS analyses of the measured samples revealed a pure sample for $U_6Nb_4Al_{43}$ and an almost pure sample for UNb_2Al_{20} containing few traces of UAl_4 and $NbAl_3$ which are estimated to be less than 3% of the sample volume.

Both UNb_2Al_{20} and $U_6Nb_4Al_{43}$ can be viewed as cage-like compounds. In UNb_2Al_{20}, U-atoms are coordinated by 16 Al atoms in a Friauf polyhedron with U-Al distances ranging from 3.188(1) to 3.205(1) Å. The resulting U-U distances are 6.376(1) Å. In $U_6Nb_4Al_{43}$, U atoms have a coordination number of 17, composed of 15 Al atoms at distances ranging from 3.047(2) to 3.476(2) Å, 1 U atom at 3.412(1) Å and 1 Nb-atom at 3.555(1) Å. Along the c-axis U atoms form infinite dimeric chains with alternative U-U distances of 3.412(1) Å and 5.553(1)Å, that are slightly corrugated. The U atom separations between two adjacent chains amount to 5.556(1) Å and 6.214(1) Å.

4.3.1. UNb_2Al_{20}

The thermal dependence of the magnetic susceptibility of UNb_2Al_{20} is plotted in Figure 6. Its absolute value and very weak temperature dependence fit well with the Pauli paramagnetic behavior already reported for the isostructural UT_2Al_{20} (T = Ti, V, Cr, Mo, W) compounds [43-45]. A stretched shoulder centered approximately at 40 K is observed. Such a shoulder is encountered in uranium based spin fluctuators such as UAl_x (x = 2, 3 and 4) [46-49] or UT_2Al_{10} (T = Fe, Ru) [50, 51] as well as in UTi_2Al_{20} where it was considered as an intrinsic behavior of the phase [45]. However, it is not clear yet if this shoulder could be related (i) to the presence of one of the former binary uranium aluminides as impurity, despite the fact that they exhibit their broad maximum above 100 K, or (*ii*) to an intrinsic behavior like that observed in the latter compounds, where U-atoms are also embedded in a large cage with U-ligand distances exceeding the sum of the metallic radii of the elements. The upturn of χ(T) below 10 K is often encountered in polycrystalline 1-2-20 or 1-2-10 samples and is attributed to the presence of localized Curie-Weiss like impurities. The inset to Figure 6 presents the magnetic field dependence of UNb_2Al_{20} magnetization measured at T = 2 K. As expected for a paramagnet, a linear and fully reversible shape is described up to B = 5 T.

Please insert here Figure 6 and Figure 7.

The absence of magnetic ordering or other transition down to 1.8 K is confirmed by the specific heat measurements (Fig. 7) where no anomaly appears down to this lowest temperature of measurements. The high temperature value of C_p is not saturated at 300 K and is still far from the Dulong and Petit limit expected for 23 atoms per formula unit (573 $J.mol^{-1}.K^{-1}$). Non saturated values were also reported by Swatek *et al.* [44] for UCr_2Al_{20} at this temperature. Up to approximately 12 K, a linear behavior of $Cp/T = f(T^2)$ (inset to figure 7) is used to derive the Sommerfeld coefficient, γ = 60 $mJ.mol^{-1}.K^{-2}$ and the Debye temperature θ_D = 381 K from the Debye model:

$$\frac{C_P}{T} = \gamma + \frac{12\pi^4 R}{5\theta_D^3} T^2 \qquad \text{(II)}$$

The moderate value of the Sommefeld coefficient, highlighting moderate electron correlations, and the Debye temperature are in line with the results reported for the Pauli paramagnet UCr_2Al_{20} (γ = 80 mJ mol-1 K-2 and θ_D = 374 K [44]) while the conduction electron contribution is significantly higher in the magnetically ordered UMn_2Al_{20} (γ = 300 mJ $mol^{-1}K^{-2}$

and θ_D = 337 K) [52]. A contribution of the Cr *3d* electrons at the Fermi level, enhancing the γ-value, is nevertheless evidenced in the former case. A similar increase of the Sommerfeld coefficient with increasing electron localization has also been reported in the isostructural UT_2Zn_{20} family between the Pauli (for *T* = Fe and Ru with γ = 171 and 194 $mJ.mol^{-1}.K^{-2}$, respectively) and the Curie-Weiss paramagnets (for *T* = Co, Rh, Ir with γ = 350, 250 and 400 $mJ.mol^{-1}.K^{-2}$, respectively) [53].

Both magnetic and specific heat measurements indicate a strong delocalization, and thus a strong hybridization, of the 5*f* states in UNb_2Al_{20}.

4.3.2 $U_6Nb_4Al_{43}$

The thermal dependence of $U_6Nb_4Al_{43}$ magnetic susceptibility is plotted in Fig. 8. Above 25 K, the susceptibility follows a modified Curie Weiss law, as illustrated by the fit of the data according to Eq. (III) :

$$\frac{1}{\chi} = \frac{1}{\chi_0 + \frac{\mu_{eff}^2}{8(T-\theta_p)}} \qquad \text{(III)}$$

where χ_0 is a temperature-independent term accounting for the Pauli paramagnetism of conductin electron and core diamagnetism, θp is the paramagnetic Weiss temperature and μ^{eff} is the effective moment. The fit of χ^{-1}(T) to Eq. (III) results (Fig. 8a) in the following values : χ_0 = 8.02(7) 10^{-4} $emu.mol_U^{-1}$, θp = -134 (1) K and μ^{eff} = 2.38 μ_B, . The value of the effective moment is in the order of magnitude usually encountered in uranium based intermetallics and the large negative value of θp suggests the dominance of antiferromagnetic exchange interactions, but may also refer to strong delocalization of the 5*f* states.

Please insert here Fig. 8.

The low temperature of the χ(T) curve displays a small magnitude two-step increase below 12(1) K and 7(1) K, respectively, in the field cooled (FC) mode and a cusp at 12 K in the zero field cooled (ZFC) mode. Both the precis microstructural examination of the polycrystalline sample and the absence of any magnetically ordered phases in the U-Nb-Al phase diagram rule out the possibility of an impurity origin for these magnetic signals. The ZFC-FC mode hysteresis is in agreement with the M(B) measurements performed at T = 2 K (Fig. 8b), where the first magnetization curve (open symbols) shows a linear increase of the

magnetization with the applied magnetic field, while the subsequent demagnetization curve also follows a linear decrease but with a slightly different slope resulting in a small remanence at B = 0 T of about 10^{-3} μ_B per U-atom. In order to better characterize this magnetic feature, χ(T) has been measured under different applied magnetic fields lower than 5000 Oe (Fig. 8c). Three main features can be observed, (*i*) a small disruption in the ZFC-FC modes opening between 12-9K, which shifts to lower temperature with increasing applied field, followed by (*ii*) a marked opening below 7 K and (*iii*) a broad maximum or shoulder (FC and ZFC) centered at T = 12 K. The latter two anomalies are independent from the applied magnetic field. Such complex behavior of the susceptibility may be compatible with a scheme involving short-range and long-range magnetic orderings, with assumed competitions. In this respect, the large difference between the θp absolute value and the ordering temperature, of more than one order of magnitude, reflects strong frustrations.

Puzzling magnetic phases and multiple magnetic transitions at low temperature are often encountered in the isostructural $RE_6T_4Al_{43}$ (*RE* = rare earth; *T* = transition metal) compounds showing mainly antiferromagnetic interactions such as in $Sm_6Ta_4Al_{43}$ [54] $Gd_6Cr_4Al_{43}$, [55] and $Gd_6T_4Al_{43}$ (T = Cr, Mo, W) [56]. This is the case for $Tm_6Cr_4Al_{43}$, for which Fushiya *et al*. [57] discuss this ordering by considering the formation of magnetic dimers between the two closest magnetic atoms (d(U-U) = 3.412(1) Å in $U_6Nb_4Al_{43}$) , mutually separated by a much larger distance, and the subsequent competition between intra- and inter-dimer magnetic interactions. Within the $Ho_6Mo_4Al_{43}$ structure type, the dimers are aligned more or less along the *c*-axis (Fig. 9). The distance between the dimers is about 5.5 Å both within the chains and between two adjacent chains. Such a competition between intra- and inter-dimers is wildly studied in low-dimensional molecular magnet based on *d*-metal complexes, but is more rarely encountered in *f*-metal intermetallics. A related interesting example of magnetic dimershas been debated in the case of *e.g*. Yb_2Pt_2Pb, which shows a composite magnetic behavior [58] involving antiferromagnetic order and strong magnetic frustration resulting from a Shastry-Sutherland network [59].

Please insert here Figure 9.

The intrinsic nature of the magnetic transition is confirmed by the specific heat and electrical resistivity measurements (Fig. 10). The Cp/T=f(T^2) curve (inset to Fig. 10(a)) shows a peak around 150 K^2 corresponding to the broad maximum from the susceptibility data (T =

12(1) K). This peak does not vanish at lower temperature but extends almost to the lowest measured temperature (1.8 K), probably due to the superimposition of a second signal corresponding to the second magnetic transition. An estimation of the Sommerfeld coefficient $\gamma \approx 800$ mJ mol^{-1} K^{-2} (or 133 mJ mol_U^{-1} K^{-2}) can be obtained by extrapolating the linear behavior of $Cp/T=f(T^2)$ above 150 K^2 (12.24 K), highlighting much stronger electronic correlations in this aluminide compared to the former one.

The temperature dependence of the electrical resistivity is plotted in Fig. 10(b). In the paramagnetic region ρ(T) slightly decreases with decreasing temperature, with a weak curvature centered around 175 K, reflecting electron phonon interactions or spin-fluctuations. Below 11 K, ρ(T) undergoes a pronounced decrease with a sharp inflection at 7.5 K, expected from a lower scattering of the electrons in the magnetically ordered long-range state. Below 7.5 K, ρ(T) can be described by an equation comprising both a Fermi-Liquid and an antiferromagnetic spin-wave terms [60].

$$\rho(T) = \rho_0 + b.T.\left(1 + \frac{2.T}{\Delta}\right)\exp\left(-\frac{\Delta}{T}\right) + cT^2 \qquad \text{(IV)}$$

where ρ_0 is the residual resistivity, Δ is a gap in the spin-waves spectrum and *b* and *c* are coefficients of proportionality. Fits of Eq.(IV) (inset to Fig. 10b) below 7.5 K to the experimental data yielded the values, ρ_0 = 126.40(5) μΩ.cm, $\Delta = 39(5)$ K, b = 62(39) μΩ.cm.K^{-1} and c = 0.168(1) μΩ.cm.K^{-2}. The values obtained compare reasonably well the ones obtained for URu_2Si_2 [60].

5. Conclusion

The present work about the U-Nb-Al system is a part of a systematic investigation of U-*T*-Al ternary systems, where *T* = Mo, Ti, Zr [40, 61, 62] and Nb. These four transition elements display extensive solid solubility in the γU phase at elevated temperature. Of this group, Nb is somewhat unique in that the U-Nb binary system does not show an intermediate phase and presents a miscibility gap at moderate temperature. Unlike for our previous studies, a combined approach of the experimental assessment of the isothermal sections at 900 K and 1200 K with their thermodynamic assessment by the CALPHAD method has been conducted in the present investigation.

Two isothermal sections of the U-Nb-Al ternary system were established for the entire concentration range. They have been constructed using typical experimental techniques by combining the results of SEM-EDS and XRD analyses of annealed samples at 900 K and at 1200 K. The major difficulties of the experimental assessment lie in the low atomic diffusion and grain growth, especially in the vicinity of the Nb-rich side. At 900 K, to overcome these drawbacks, a prolonged three-month heat treatment was necessary.

The isothermal sections in the Al-poor region are dominated by phase equilibria involving the Nb_2Al (σ-phase). Its extension into the ternary sections was found to evolve markedly with the temperature, with U-solubilities of about 6(1), 10(1) and 12.5(1) at. % U at 900K, at 1200K and for as-cast samples, respectively. To more precisely determine the substitution mechanism, XRD experiments on single crystal were performed. The refinement of the crystal structure shows that the U substitutes Nb on the *4g* Wyckoff site of the $P4_2/mnm$ space group. As expected from the comparison of the metallic radii, an increase of the cell volume is observed but with anisotropic effects between the basal plane (decrease) and the orthogonal plane (increase) compared to the non-substituted binary phase.

In the Al-rich part of the ternary system, the formation of UNb_2Al_{20} and $U_6Nb_4Al_{43}$ was confirmed. They remain stable down to room temperature. They both decompose by peritectic reactions: $UNb_2Al_{20} \rightarrow NbAl_3 + U_6Nb_4Al_{43} + L$ at 1200(5) K and $U_6Nb_4Al_{43} \rightarrow UAl_3 + NbAl_3 + L$ at 1262(5) K. These reaction schemes are consistent with both the experimental observations and the thermodynamic modeling. Their crystal structure was refined from single crystal diffraction data. UNb_2Al_{20} adopts the $CeCr_2Al_{20}$ structure type (cubic, $Fd\bar{3}m$, n°227) with lattice parameter at room temperature, *a* = 14.772(1) Å. A small deviation from the stoichiometry is observed, yielding the crystallographic formula $UNb_{1.9}Al_{20.1}$. $U_6Nb_4Al_{43}$ crystallizes with the $Ho_6Mo_4Al_{43}$ structure type (hexagonal, $P6_3/mcm$, n° 193) with lattice parameters at room temperature, *a* = 11.064(1) Å and *c* = 17.825(1) Å. Unlike most of the isotypic aluminides, these ternary phases should be regarded as line compounds.

The modeling of these isothermal sections was carried out by the Calphad method, allowing reproduction with rather good agreement of the experimental composition limits and the equilibrium relations of the U-Nb-Al system at both temperatures, 900 K and 1200 K. The main discrepancies with experimental measurements lie in a too-rich Nb content for the *bcc* phases (Nb and γU) in equilibrium with the ternary extension of Nb_2Al (σ-phase). This phenomenon can be ascribed to the interaction parameters in the binary U-Nb system. The

assessed ternary thermodynamic parameters were used to calculate the liquidus projection and the invariant reactions along with their corresponding temperatures, which are given to complete the description of the U-Nb-Al phase diagram. They are both in agreement with the experimental information regarding the solidification of the unary and binary phases and with the formation of $U_6Nb_4Al_{43}$ and UNb_2Al_{20}. More precise description of both the surfaces of the primary solidification and invariant reactions would require experimental verification allowing to introduce interaction parameters in the thermodynamic optimization of the liquid phase.

The electronic properties of both intermediate compounds were measured by means of *dc*-magnetic susceptibility, specific heat and resistivity measurements in the temperature range 2-300K, revealing that UNb_2Al_{20} has to be regarded as an enhanced Pauli paramagnet showing a shoulder like susceptibility feature at about 40 K referring to some possible spin fluctuations. $U_6Nb_4Al_{43}$ displays non-trivial magnetic ordering at low temperature with a two-step mechanism. Below T =7 K, the ρ(T) and χ(T) recorded under low applied field would suggest a magnetic ground state dominated by antiferromagnetism. However, in the temperature range 12 - 7 K, a composite behavior involving long-range interactions and magnetic frustration is suspected. The origin of the phenomenon may lie in the formation of U-U dimeric infinite chains running along the *c*-axis, yielding possible intra and inter couplings. Subsequent microscopic study on single crystal would be highly desirable to check the strong magnetic anisotropy suspected between the *c*-axis and the basal (*a*,*b*) plane.

Acknowledgement.

The authors wish to thank the Centre de Microscopie Électronique à Balayage et microAnalyse (CMEBA) for complementary SEM-EDS analyses. We also thank Z. El Sayah for some syntheses and S. Fryars for her precious role in the management of the U samples.

Supporting Information.

Crystallographic files in cif format for $U_{0.08}Nb_{1.95}Al_{0.97}$, $UNb_{1.9}Al_{20.}$ and $U_6Nb_4Al_{43}$ are provided. The thermodynamic database file (TDB file) is provided as “supplementary materials”.

References:

[1] M. Anagnostidis, M. Colombié, H. Monti, Phases métastables dans les alliages uranium-niobium. *J. Nucl. Mater*., 11 (1964) 67-76.

[2] C. d'Amato, F.S. Saraceno, T.B. Wilson, Phase transformations and equilibrium structures in uranium rich niobium alloys. *J. Nucl. Mater*., 12 (1964) 291-304.

[3] K. Tangri, D.K. Chaudhuri, Metastable phases in uranium alloys with high solute solubility in the bcc gamma phase. Part I – the system U-Nb. *J. Nucl. Mater*., 15 (1964) 278-287.

[4] R.A. Vandermeer, Phase transformations in a uranium + 14 at.% niobium alloy. *Acta Metallurgica*, 2b (1980) 383-393.

[5] K.H. Eckelmeyer, A.D. Romig, L.J Weirick, The effect of quench rate on the microstructure, mechanical properties, and corrosion behavior of U-6 Wt Pct Nb. *Metall Trans A*, 15 (1984)1319-1330

[6] H.M. Volz, R.E. Hackenberg, A.M.Kelly, W.L. Hults, A.C. Lawson, R.D. Field, D.F. Teter, D.J. Thoma, X-ray diffraction analyses of aged U–Nb alloys. *J. Alloys Compd*., 444-445 (2007) 217-225.

[7] S. Niemann, W. Jeitschko, Ternary aluminides AT_2Al_{20} (A = Rare Earth Elements and Uranium; T = Ti, Nb, Ta, Mo, and W) with $CeCr_2Al_{20}$-type structure. *J. Solid State Chem*., 114 (1995)337-341.

[8] S. Niemann, W. Jeitschko, Ternary aluminides $A_6T_4Al_{43}$ (A= Y, Nd, Sm, Gd-Lu, and U; T= Ti, V, Nb, and Ta) with $Ho_6Mo_4Al_{43}$ type structure. *J. Solid State Chem*., 116 (1995) 131-135.

[9]) H.R. Ott, H. Rudigier, Z. Fisk, J.L Smith, UBe_{13}: an unconventional actinide superconductor. *Phys. Rev. Lett*., 50 (1983)1595-1598.

10]) W. Kraus, , G. Nolze, PowderCell for Windows Version 2.4, Federal Institute for Materials Research and Testing, Berlin (8.03.2000).

[11] J. Rodriguez-Carvajal, Recent advances in magnetic structure determination by neutron powder diffraction. *Physica B*, 192 (1993) 55-69.

[12] Brüker-AXS, In: Collect, Denzo, Scalepack, Sortav. Kappa CCD Program Package, Delft, The Netherlands, 1998.

[13] A. Altomare, M.C. Burla, M. Camalli, G.L. Cascarano, C. Giacovazzo, A. Guagliardi, A.G.G. Moliterni, G. Polidori, R. Spagna, SIR97: a new tool for crystal structure determination and refinement. *J. Appl. Crystallogr*., 32 (1999) 115-119.

[14] G.M. Sheldrick, Crystal structure refinement with SHELXL. *Acta Crystallogr*. Sect C, 71 (2015) 3-8.

[15]) E. Parthé, K. Cenzual, R. Gladyshevskii, Standardization of crystal structure data as an aid to the classification of crystal structure types. *J. Alloys Compd*., 197 (1993) 291-301.

[16] J-O. Andersson, T. Helander, L. Höglund, P. Shi, P.B. Sundman, Thermo-Calc & DICTRA, computational tools for materials science, 26 (2002)273–312.

[17] T.B. Massalski, H. Okamoto, P.R. Subramanian, L. Kacprzak L. (Eds.), Binary Alloy Phase Diagrams, vols. 1–3, second ed., ASM International, 1990.

[18] M.E. Kassner, P.H. Adler, M.G. Adamson, D.E. Peterson, Evaluation and thermodynamic analysis of phase equilibria in the U-Al system. *J. Nucl. Mater*., 167 (1989) 160-168.

[19] O. Tougait, H. Noël, Stoichiometry of UAl_4. *Intermetallics*, 12 (2004) 219-223.

[20] X. Zhang, Y.F. Cui, G.L. Xu, W.J. Zhu, H.S. Liu, B.Y. Yin, Z.P. Jin, Thermodynamic assessment of the U–Mo–Al system. *J. Nucl. Mater*., 420 (2010) 15-24.

[21] J. Koike, M.E. Kassner, R.E. Tate, R.S. Rosen, The Nb-U (niobium-uranium) system. *J. Phase Equilibria*, 19 (1998) 2253-2260.

[22] H.A. Saller, F.A. Rough, Compilation of US and UK uranium and thorium constitutional diagrams. US Atomic Energy Commission. Publication BMI-1000, (1955).

[23] X.J. Liu, Z.S. Li, J. Wang, C.P. Wang, Thermodynamic modeling of the U–Mn and U–Nb systems. *J. Nucl. Mater*., 380 (2008) 99-104.

[24] J.L. Jorda, R. Flükiger, J.A Muller, new metallurgical investigation of the niobium-aluminium system. *J. Less-common Met*., 75 (1980) 227-239.

[25] L. Kaufman, Calculation of multicomponent tantalum based phase diagrams. *Calphad,* 15 (1991) 261-282

[26] C. Servant, I. Ansara, Thermodynamic assessment of the Al-Nb system. *J. Chim. Phys*., 97 (1997) 869-888.

[27] Z. Zhu, Y. Du, L. Zhang, H. Chen, H. Xu, C. Tang, Experimental identification of the degenerated equilibrium and thermodynamic modeling in the Al–Nb system. *J. Alloys Compd*., 460 (2008) 632-638.

[28] V.T. Witusiewicz, A.A. Bondar, U. Hecht, T.Y. Velikanova, The Al–B–Nb–Ti system: IV. Experimental study and thermodynamic re-evaluation of the binary Al–Nb and ternary Al–Nb–Ti systems. *J. Alloys Compd.*, 472 (2009) 133-161.

[29] C. He, F. Stein, M. Palm, Thermodynamic description of the systems Co–Nb, Al–Nb and Co–Al–Nb. *J. Alloys Compd*., 637 (2015) 361-375.

[30] F.H. Ellinger, R.O. Elliott, E.M. Cramer, The plutonium - uranium system. *J. Nucl. Mater*., 1 (1959) 233-243.

[31] C.W. Tucker Jr, P. Senio, An improved determination of the crystal structure of β-uranium. *Acta Crystallogr*., 6 (1953) 753-760.

[32] A.S. Wilson, R.E Rundle, The structures of uranium metal, *Acta Crystallogr*., 2 (1949) 126-127.

[33] H. Bückle, Aufbau und Mikrohärte der Zwei- und Dreistoffsysteme der Metalle Niob, Tantal, Molybdän und Wolfram, *Z. Metalkd*., 37 (1946) 53-56.

[34] G. Grube, L. Botzenhardt, Die Legierungen des Thoriums mit Kupfer, Aluminium und Natrium, *Z. Elektrochem. Angew. Phys. Chem*., 48 (1942) 418-425.

[35] S. Steeb, G. Petzow, Strukturelle Veränderungen der Laves-Phasen $ZrAl_2$ und UAl_2 durch Uran-bzw. Zirkonzusätze. *Naturwissenschaften*, 48 (1961) 450-451.

[36] E.A. Wood, V.B. Compton, B.T. Matthias, E. Corenzwit, β-Wolfram structure of compounds between transition elements and aluminum, gallium and antimony. *Acta Crystallogr.*, 11 (1958) 604-606.

[37] E.I. Gladyshevskii, Crystal structure of the compound Nb_2Al. *J. Struct. Chem*., 2 (1961) 148-151.

[38] G. Brauer, Über die Kristallstruktur von $TiAl_3$, $NbAl_3$, $TaAl_3$ und $ZrAl_3$ *Z. Anorg. Allg. Chem*., 242 (1939) 1-22.

[39] J-M. Joubert, Crystal chemistry and Calphad modeling of the σ phase. *Prog. Mater. Sci*., 53 (2008) 528-583.

[40] H. Noël, O. Tougait, S. Dubois, Phase relations in the U–Mo–Al ternary system. *J. Nucl. Mater*., 389 (2009) 93-97.

[41] V.M.T. Thiede, W. Jeitschko, S. Niemann, T. Ebel, $EuTa_2Al_{20}$, Ca W_4Al_{43} and other compounds with $CeCr_2Al_{20}$ and $Ho_6Mo_4Al_{43}$ type structures and some magnetic properties of these compounds. *J. Alloys Compd*., 267 (1998) 23–31.

[42] S. Niemann, W. Jeitschko, Ternary aluminides $A_6T_4Al_{43}$ with A= Y, Nd, Sm, Gd-Lu, Th, U and T= Cr, Mo, W. *Z. Metallkd*., 85 (1994) 345-349.

[43] I. Halevy, E. Sterer, M. Aizenshtein, G. Kimmel, D. Regev, E. Yahel, L.C.J. Pereira, A.P. Goncalves, High pressure studies of a new ternary actinide compound, UV_2Al_{20}. *J. Alloys Compd*., 319 (2001) 19-21.

[44] P. Swatek, D. Kaczorowski, Magnetic and electrical properties of UCr_2Al_{20} single crystals. *J. Solid State Chem*., 191 (2012) 191-194.

[45] Y. Matsumoto, T.D. Matsuda, N. Tateiwa, E. Yamamoto, Y. Haga, Single crystal growth and physical properties of UT_2Al_{20} (T= Transition Metal). *J. Korean Phys. Soc*., 63 (2013) 363-366.

[46] M.R. Brodsky, R.J. Trainor, Band magnetism due to f-electrons. *Physica B*, 91 (1977) 271-277.

[47] I. Lupşa, P. Lucaci, E. Burzo, Magnetic properties of $U(Co_xAl_{1-x})_3$ compounds. *J. Alloys Compd.*, 204 (1994) 247-250.

[48] E. Burzo, P. Lucaci, I. Lupşa, Magnetic properties of $U(Al_{1-x}Co_x)_4$ compounds. *J. Magn. Magn. Mater.*, 140 (1994) 1413-1414.

[49] D. Aoki, Y. Haga, Y. Homma, Y. Shiokawa, E. Yamamoto, A. Nakamura, R. Settai, Y. Ōnuki, Magnetic and electrical properties in $NpAl_4$ and UAl_4. *J. Phys. Soc. Jpn*., 78 (2009) 044712.

[50] T. Sugai, Y. Haga, T.D. Matsuda, E. Yamamoto, N. Tateiwa, F. Honda, R. Settai, Y. Ōnuki, Single crystal growth and physical properties of ternary uranium compounds UM2Al10 (M=Fe, Ru and Os). *J. Phys.:Conf. Ser.*, 273 (2011) 012122.

[51] R. Troć, M. Pasturel, O. Tougait, M. Potel, H. Noël, Crystal structure and physical properties of a new intermetallic compound URu_2Al_{10}. *Intermetallics*, 19 (2011) 913-918.

[52] C.H. Wang, J.M. Lawrence, E.D. Bauer, K. Kothapalli, J.S. Gardner, F. Ronning, K. Gofryk, J.D. Thompson, H. Nakotte, F. Trouw, Unusual signatures of the ferromagnetic transition in the heavy fermion compound UMn_2Al_{20}. *Phys. Rev. B*, 82 (2010)094406.

[53] P. Swatek, D. Kaczorowski, Heavy fermion behavior in UT_2Zn_{20} (T= Fe, Co, Ru, Rh, Ir) Compounds. *J. Phys. Soc. Jpn*., 80 (2011)SA106.

[54] M.W. Wolff, S. Niemann, T. Ebel, W. Jeitschko, Magnetic properties of rare-earth transition metal aluminides $R_6T_4Al_{43}$ with $Ho_6Mo_4Al_{43}$-type structure. *J. Magn. Magn. Mater*., 223 (2001)1-15.

[55] Yu. Verbovytsky, K. Łątka, K. Tomala, The crystal structure and magnetic properties of the GdV_2Al_{20} and $GdCr_2Al_{20}$ ternary compounds. *J. Alloys Compd*., 450 (2008), 114-117.

[56] M.J. Kangas, L-R. J. Treadwell, N. Haldoaarachchige, J.D. McAlpin, D.P. Young, J.Y. Chan, Magnetic and electrical properties of flux grown single crystals of $Ln_6M_4Al_{43}$ (Ln= Gd, Yb; M= Cr, Mo, W). *J. Solid State Chem*., 197 (2013) 523-531.

[57] K. Fushiya, R. Miyazaki, R. Higashinaka, T.D. Matsuda, Y. Aoki, Single crystal growth and anisotropic magnetic properties of peanut-shaped cage compound $Tm_6Cr_4Al_{43}$. *JPS Conf. Proc.*, 3 (2014) 011018.

[58] M.S. Kim, M.C. Aronson, Spin liquids and antiferromagnetic order in the Shastry-Sutherland-lattice compound Yb_2Pt_2Pb. *Phys. Rev. Lett*., 110 (2013) 017201 1-6.

[59] B.S. Shastry, B. Sutherland, Exact ground state of a quantum mechanical antiferromagnet. *Physica B*, 108 (1981) 1069-1070.

[60] T. T. M. Palstra, A. A. Menovsky, J. A. Mydosh, Anisotropic electrical resistivity of the magnetic heavy-fermion superconductor URu_2Si_2, Phys; Rev. B 33 (1986) 6527.

[61] C. Moussa, M. Pasturel, B. Stepnik, O. Tougait, O. Experimental study of phase relations in the U–Ti–Al ternary system. *Intermetallics*, 57 (2015) 1-6.

[62] C. Moussa, F. Désévédavy, H. Noël, M. Pasturel, F. Gouttefangeas, S. Dubois, B. Stepnik, O. Tougait, Experimental investigation of the U–Zr–Al ternary phase diagram: Isothermal sections at 673K and 1073K. *J. Nucl. Mater.*, 461 (2015) 193–199.

Table captions:

Table 1: Crystallographic data, along with the stability domain and the homogeneity range of the unary and binary phases involved in the U-Nb-Al system.

Table 2: Phase compositions (in at.%) in the three-phase fields as well as some tie-lines used to ascertain various solubilities in the isothermal section at 900 K. All EDS figures are given with an error of ± 0.5 at. %. (*NA: not accurate due to too small size grains.)

Table 3: Phase compositions (in at.%) in the three-phase fields as well as some tie-lines used to ascertain various solubilities in the isothermal section at 1200 K. All EDS figures are given with an error of ± 0.5 at. %. (*NA: not accurate due to too small size grains.)

Table 4 Homogeneity ranges of the Nb-Al phases at 1200K**.**

Table 5: Single Crystal data and structure refinement parameters.

Table 6: Positional and equivalent isotropic thermal displacement parameters ($Å^2$) for $U_{0.08}Nb_{1.95}Al_{0.97}$

Table 7: Evolution of the lattice parameters of the $U_xNb_{2-x+y}Al_{1-y}$ phase upon increasing the U solubility compared to the pure binary phase (Nb_2Al).

Table 8: Positional and equivalent isotropic thermal displacement parameters ($Å^2$) for $UNb_{1.9}Al_{20.1}$

Table 9: Positional and equivalent isotropic thermal displacement parameters ($Å^2$) for $U_6Nb_4Al_{43}$

Table 10: Model and optimized thermodynamic parameters of the U-Nb-Al ternary system in bold, other parameters are taken from [20, 23, 29]..

Table 11: Calculated invariant reactions and temperatures of the U-Nb-Al ternary system.

Figure captions:

Figure 1: Experimental isothermal section at 900 K of the U-Nb-Al ternary system. The black solid lines delimit the three-phase fields. The thin dotted lines represent the tie-lines. The grey areas correspond to the homogeneity domains of the unary and binary phases. The symbols φ_1 and φ_2 stand for $U_6Nb_4Al_{43}$ and UNb_2Al_{20} respectively.

Figure 2: Experimental isothermal section at 1200 K of the U-Nb-Al ternary system. The black solid lines delimit the three-phase fields. The thin dotted lines represent the tie-lines. The grey areas correspond to the homogeneity domains of the unary and binary phases. The thick dotted line stands for the equilibrium with the liquid phase which was not determined. The symbol φ_1 stands for $U_6Nb_4Al_{43}$.

Figure 3: Calculated isothermal section at 900 K of the U-Nb-Al ternary system. The red solid lines stand for the equilibrium lines delimiting the three-phase fields. The green lines represent the tie-lines.

Figure 4: Calculated isothermal section at 1200K of the U-Nb-Al ternary system. The red solid lines stand for the equilibrium lines delimiting the three-phase field. The green lines represent the tie-lines.

Figure 5: Calculated liquidus projection of the U-Nb-Al ternary system. The red solid lines correspond to the liquid paths.

Figure 6: Thermal dependence of UNb_2Al_{20} magnetic susceptibility. The inset plots the magnetic field dependence of the magnetization isotherm at T = 2 K.

Figure 7: Thermal dependence of the UNb_2Al_{20} specific heat. The inset shows the low temperature domain of $C_P/T = f(T^2)$.

Figure 8 (a) Thermal dependence of $U_6Nb_4Al_{43}$ magnetic susceptibility (left) and its inverse (right) measured in the ZFC (open) and FC (full symbols) modes. The red line corresponds to the modified Curie-Weiss fit to $\chi^{-1}(T)$. (b) Magnetic field dependence of $U_6Nb_4Al_{43}$ magnetization isotherm measured at 2 K upon increasing (open) and decreasing (full symbols) magnetic field. (c) Low temperature part of $\chi(T)$ curves measured in the ZFC (open) and Fc (full symbols) under various applied magnetic fields.

Figure 9: U-atom lattice in the $U_6Nb_4Al_{43}$ unit cell showing the formation of U-U dimers (solid lines) and the U spacing of 5.55(1) Å (dotted lines) for inter and intra chains.

Figure 10: Thermal dependence of $U_6Nb_4Al_{43}$ (a) heat capacity and (b) electrical resistivity. The inset to panel (a) plots the T^2 dependence of C_p/T. The insets to panel (b) shows the fit of the experimental data according to Eq (IV).

Titre:

The U-Nb-Al ternary system: experimental and simulated investigations of the phase equilibria and study of the crystal structure and electronic properties of the intermediate phases.

Auteurs:

Chantal Moussa[1], Alexandre Berche[1], Mathieu Pasturel[1], José Barbosa[1], Bertrand Stepnik[2], Sylvie Dubois[3] and Olivier Tougait[1,4]

Affiliation:

[1]*Institut des Sciences Chimiques de Rennes, UMR CNRS 6226, Université Rennes 1, Campus de Beaulieu, 35042 Rennes Cedex, France*

2 *AREVA/CERCA, 10 Rue Juliette Récamier, 69006 Lyon – France*

3 CEA/DEN/DEC, Cadarache, 13108 St. Paul Lez Durance, France.

[4]*Unité de Catalyse et de Chimie du Solide, UMR CNRS 8181, Université de Lille, 59695 Villeneuve d'Ascq, France*

Corresponding author : Olivier TOUGAIT, Unité de Catalyse et de Chimie du Solide, UMR CNRS 8181, Université de Lille, 59695 Villeneuve d'Ascq, France.

Email : tougait@univ-rennes1.fr

TABLES

Table 1: Crystallographic data, along with the stability domain and the homogeneity range of the unary and binary phases involved in the U-Nb-Al system.

Phase	Structure type	Space group	Lattice parameters (Å)			Domain of stability (K)	Composition range (900K)	Composition range (1200K)	ref
			a	b	c				
αU	αU	*Cmcm*	2.8542	5.8667	4.9540	< 941	< 1 at.% Nb		30, 21
βU	βU	*$P4_2/mnm$*	10.7590	-	5.6560	1049-941			31
γU	W	$Im\bar{3}m$	3.4900	-	-	1408-1049		2.5 at.% Al 37 at.% Nb	32, 17, 21
Nb	W	$Im\bar{3}m$	3.3003	-	-	< 2742	9 at. % Al 29 at % U	9 at. % Al 38 at.% U	33, 24 21
Al	Cu	$Fm\bar{3}m$	4.0410	-	-	<933			34
UAl_2	$MgCu_2$	$Fd\bar{3}m$	7.7763	-	-	<1893			35
UAl_3	Cu_3Au	$Pm\bar{3}m$	4.2660	-	-	<1623			19
UAl_4	UAl_4	*Imma*	4.4014	6.2552	13.7279	<1004			19
Nb_3Al	Cr_3Si	$Pm\bar{3}n$	5.187	-	-	< 2333	18.5 – 21.8 at. % Al	18.5 – 21.8 at. % Al	36 24
Nb_2Al	Nb_2Al	*$P4_2/mnm$*	9.957	-	5.167	< 2207	30.0 – 34.5 at. % Al	30.0 – 34.5 at. % Al	37 24
$NbAl_3$	$TiAl_3$	*I4/mmm*	3.838	-	8.584	< 1961			38

Table 2: Phase compositions (in at.%) in the three-phase fields as well as some tie-lines used to ascertain various solubilities in the isothermal section at 900 K. All EDS figures are given with an error of ± 0.5 at. %. (*NA: not accurate due to too small size grains.)

Sample	Phase field domain (XRD)	Phase composition (SEM-EDS)		
1U-14Nb-85Al	Al+UNb_2Al_{20}+$NbAl_3$	Al: 100Al	UNb_2Al_{20}: 5U-7Nb-88Al	$NbAl_3$: 26Nb-74Al
7U-3Nb-90Al	Al+UNb_2Al_{20}+UAl_4	Al: 100Al	UNb_2Al_{20}: 5U-7Nb-88Al	UAl_4: 20U-80Al
13U-4Nb-83Al	UAl_3+UNb_2Al_{20} +$U_6Nb_4Al_{43}$	UAl_3: 25U-75Al	UNb_2Al_{20}: 5U-7Nb-88Al	$U_6Nb_4Al_{43}$: 12U-7Nb-81Al
5U-13Nb-82Al	$NbAl_3$+UNb_2Al_{20} +$U_6Nb_4Al_{43}$	$NbAl_3$: 25Nb-75Al	UNb_2Al_{20}: 5U-7Nb-88Al	$U_6Nb_4Al_{43}$: 12U-7Nb-81Al
7U-17Nb-76Al	UAl_3+$NbAl_3$	UAl_3: 25U-75Al	$NbAl_3$: 26Nb-74Al	
15U-11Nb-74Al	UAl_3+UAl_2+$NbAl_3$	UAl_3: 25U-75Al	UAl_2: 34U-66Al	$NbAl_3$: 26Nb-74Al
31U-38Nb-31Al	UAl_2+Nb_2Al+U	UAl_2:33U-66Al-1Nb	Nb_2Al: 5U-62Nb-33Al	U: 98U-2Al
15U-25Nb-60Al	$NbAl_3$+Nb_2Al+UAl_2	$NbAl_3$: 25Nb-75Al	Nb_2Al: 3U-64Al-33Nb	UAl_2: NA
8U-71Nb-21Al	Nb_3Al+Nb_2Al+Nb	Nb_3Al: 21Al-78Nb-1U	Nb_2Al: 5U-64Nb-31Al	Nb: 20U-78Nb-2Al
9U-79Nb-12Al	Nb_3Al+ Nb	Nb_3Al: 20Al-79Nb-1U	Nb: 15U-82Nb-3Al	
21U-55Nb-25Al	Nb_2Al+Nb+U	Nb_2Al: 31Al-64Nb-5U	Nb: NA	U:NA

Table 3: Phase compositions (in at.%) in the three-phase fields as well as some tie-lines used to ascertain various solubilities in the isothermal section at 1200 K. All EDS figures are given with an error of ± 0.5 at. %. (*NA: not accurate due to too small size grains.)

Sample	Phase field domain (XRD)	Phase composition (SEM-EDS)		
11U-5Nb-84Al	Al+$U_6Nb_4Al_{43}$+UAl_3	Al: 100Al	$U_6Nb_4Al_{43}$: 12U-7Nb-81Al	UAl_3: 25U-75Al
4U-10Nb-86Al	$NbAl_3$+$U_6Nb_4Al_{43}$+UAl_3	$NbAl_3$: 25Nb-75Al	$U_6Nb_4Al_{43}$: 12U-7Nb-81Al	UAl_3: 25U-75Al
24U-5Nb-71Al	UAl_3+UAl_2+$NbAl_3$	UAl_3: 25U-75Al	UAl_2: 33U-67Al	$NbAl_3$: 24Nb-75Al-1U
4U-45Nb-51Al	$NbAl_3$+Nb_2Al+UAl_2	$NbAl_3$: 26Nb-74Al	Nb_2Al: 59Nb-38Al-3U	UAl_2: NA
30U-34Nb-36Al	UAl_2+Nb_2Al+U	UAl_2:34U-63Al-3Nb	Nb_2Al: 12U-54Nb-34Al	U: 96U-2Nb-2Al
31U-51Nb-18Al	Nb_2Al+Nb+U	Nb_2Al: 32Al-65Nb-3U	Nb:38U-60Nb-2Al	U:60U-40Nb-0Al
28U-44Nb-28Al	U+Nb_2Al	U: 92U-7Nb-1Al	Nb_2Al: 33Al-59Nb-8U	
3U-86Nb-11Al	Nb_3Al+Nb	Nb_3Al: 1U-80Nb-19Al	Nb: 2U-91Nb-7Al	
17U-69Nb-14Al	Nb_2Al+Nb+ Nb_3Al	Nb_2Al: 32Al-65Nb-3U	Nb:38U-60Nb-2Al	Nb_3Al: 1U-80Nb-19Al

Table 4 Homogeneity ranges of the Nb-Al phases at 1200K**.**

Phase	Present work (exp)	Jorda (exp) [21]	Zhu (calc) [24]	Witusiewicz (calc) [25]	He (calc) [26]
$NbAl_3$	75	75	75	75	74.9-75.1
Nb_2Al	32-36	30-34.5	30-33	30.5-33	30-36
Nb_3Al	19-20	18.5-21.8	18-21	18-20	18.2-22.5
Nb	7	9	7.5	5	9.8

Table 5 Single Crystal data and structure refinement parameters.

Target composition	10U-60Nb-30Al	4.3U-8.7Nb-87Al	11.3U-7.5Nb-81.2Al
Refined formula	$U_{0.08}Nb_{1.95}Al_{0.97}$	$UNb_{1.9}Al_{20.1}$	$U_6Nb_4Al_{43}$
Crystal system	Tetragonal	Cubic	Hexagonal
Space group	*P4₂/mnm* (n°136)	$Fd\bar{3}m$ (n°227)	*P6₃/mcm* (n°193)
Cell parameters (Å)	a=9.901(1) c=5.258(1)	a=14.724(1)	a=11.064(1) c=17.826(1)
θ range (°)	5.83-41.97	3.91 – 41.98	3.68 – 40.00
Reflections collected / R int	16745 / 0.137	10500 / 0.0639	20741 / 0.2715
unique reflections / unique [$F^2 > 2\sigma(F^2)$] / parameters	1017 / 828 / 30	576 / 519/ 18	2125 / 1361 / 53
Reliability factors* [$F^2>2\sigma(F^2)$]	R_1=0.0433; wR_2=0.0689	R_1=0.0201; wR_2=0.0225	R_1=0.0601; wR_2=0.0772
Residual Peaks (ē.Å^{-3})	2.17 / -2.77	0.70 / -0.85	2.81 / -4.15

* $R_1 = \sum \left| |F_0| - |F_C| \right| / |F_C|$ (for $F^2>2\sigma(F^2)$)

$wR_2 = \left[\sum w(F_o^2 - F_c^2)^2 / wF_o^4\right]^{½}$, where $w^{-1} = [\sigma^2(F_o^2) + (Ap)^2 + Bp]$, $p = [\max(F_o^2, 0) + 2F_c^2]/3$

Table 6 Positional and equivalent isotropic thermal displacement parameters (Å^2) for $U_{0.08}Nb_{1.95}Al_{0.97}$

Atom	Wyckoff position	Occupancy	x	y	z	U_{eq}
U(1)	*4g*	0.204(4)	0.39816(4)	0.60184(4)	0	0.0080(2)
Nb(1)	*4g*	0.796(4)	0.39816(4)	0.60184(4)	0	0.0080(2)
Nb(2)	*8i*	1	0.13057(5)	0.53617(5)	0	0.0067(1)
Nb(3)	*8j*	1	0.31869(3)	0.31869(3)	0.2483(1)	0.0078(1)
Al(1)	*2a*	0.96(1)	0	0	0	0.013(2)
Nb(4)	*2a*	0.04(1)	0	0	0	0.013(2)
Al(2)	*8i*	0.968(5)	0.0662(2)	0.2638(2)	0	0.0094(5)
Nb(5)	*8i*	0.032(5)	0.0662(2)	0.2638(2)	0	0.0094(5)

U_{eq} is defined as one-third of the trace of the orthogonalized Uij tensor.

Table 7 Evolution of the lattice parameters of the $U_xNb_{2-x+y}Al_{1-y}$ phase upon increasing the U solubility compared to the pure binary phase (Nb_2Al).

Elemental Composition (% at.)	67Nb-33Al	60.8Nb-35.7A-3.5U	59.3Nb-33.7Al-7U
a (Å)	9.9306(1)	9.9212(3)	9.8842(5)
c (Å)	5.1777(1)	5.2260(2)	5.3019(5)
Volume (Å^3)	510.61(1)	514.40(3)	517.97(6)
$\chi 2$	1.83	3.16	3.01

Table 8 Positional and equivalent isotropic thermal displacement parameters (Å^2) for $UNb_{1.9}Al_{20.1}$

Atom	Wyckoff position	Occupancy	x	y	z	U_{eq}
U(1)	8a	1	$^1/_8$	$^1/_8$	$^1/_8$	0.00782(5)
Nb(1)	16d	0.952(3)	½	½	½	0.00474(8)
Al(1)	16d	0.048(3)	½	½	½	0.00474(8)
Al(2)	16c	1	0	0	0	0.0120(2)
Al(3)	48f	1	0.48608(4)	$^1/_8$	$^1/_8$	0.0096(1)
Al(4)	96g	1	0.06028(2)	0.06028(2)	0.32250(3)	0.01043(8)

U_{eq} is defined as one-third of the trace of the orthogonalized Uij tensor.

Table 9 Positional and equivalent isotropic thermal displacement parameters (Å^2) for $U_6Nb_4Al_{43}$

Atom	Wyckoff position	Occupancy	x	y	z	U_{eq}
U(1)	12k	1	0.52702(3)	0	0.09424(2)	0.00793(8)
Nb(1)	2b	1	0	0	0	0.0054(3)
Nb(2)	6g	1	0.72722(9)	0	$^1/_4$	0.0050(2)
Al(1)	6g	1	0.1483(4)	0	$^1/_4$	0.0096(7)
Al(2)	8h	1	$^1/_3$	$^2/_3$	0.1262(2)	0.0092(6)
Al(3)	12i	1	0.4944(3)	0.2472(2)	0	0.0099(5)
Al(4)	12j	1	0.1473(3)	0.5914(3)	$^1/_4$	0.0102(6)
Al(5)	12k	1	0.1605(3)	0	0.6146(2)	0.0106(5)
Al(6)	12k	1	0.2577(2)	0	0.02900(2)	0.0087(5)
Al(7)	24l	1	0.1600(2)	0.3959(2)	0.1624(2)	0.0102(4)

U_{eq} is defined as one-third of the trace of the orthogonalized Uij tensor.

Table 10 : Model and optimized thermodynamic parameters of the U-Nb-Al ternary system in bold, other parameters are taken from [20, 23, 29].

Phase Model	Parameters ($Jmol^{-1}$)
γ(U,Nb,Al) $(Al,Nb,U)_1(VA)_3$	${}^0L(Al,Nb,U:VA)$ = **+135 000**
UAl_2 $(U)_{0.333}(Al,Nb)_{0.667}$	$G(UAl_2,U:Nb)-0.667*{}^0H^{SER}_{Nb}-0.333*{}^0H^{SER}U$ = **+10 000** $+0.333*G^{tetra}_{U}+0.667*G^{bcc}_{Nb}$ ${}^0L(U:Al,Nb)$ = **-1 000 -1.35*T**
Nb_2Al $(Al,Nb)_{0.333}(Nb,U)_{0.134}(Al,Nb)_{0.533}$	$G(Nb_2Al,Al:U:Al)-0.134*{}^0H^{SER}_{U}-0.866*{}^0H^{SER}Al$ = **+5 004** $+0.134*G^{tetra}_{U}+0.866*G^{fcc}_{Al}$ $G(Nb_2Al,Nb:U:Nb)-0.134*{}^0H^{SER}_{U}-0.866*{}^0H^{SER}Nb$ = **+5 004** $+0.134*G^{tetra}_{U}+0.866*G^{bcc}_{Nb}$ $G(Nb_2Al,Al:U:Nb)-0.134*{}^0H^{SER}_{U}-0.333*{}^0H^{SER}Nb-0.533*{}^0H^{SER}Al$ = **-20 167 -2.4*T** $+0.134*G^{tetra}_{U}+0.333*G^{bcc}_{Nb}+0.533*G^{fcc}_{Al}$ $G(Nb_2Al,Nb:U:Al)-0.134*{}^0H^{SER}_{U}-0.533*{}^0H^{SER}Nb-0.333*{}^0H^{SER}Al$ = **+5 004** $+0.134*G^{tetra}_{U}+0.533*G^{bcc}_{Nb}+0.333*G^{fcc}_{Al}$ ${}^0L(Al:U,Nb:Nb)$ = **-6 667**
Nb_3Al $(Al,Nb,U)_{0.25}(Nb)_{0.75}$	$G(Nb_3Al,U:Nb)-0.25*{}^0H^{SER}_{U}-0.75*{}^0H^{SER}Nb$ = **5 000 -0.5*T** $+0.25*G^{tetra}_{U}+0.75*G^{bcc}_{Nb}$ ${}^0L(Al,U:Nb)$ = **-16 000**
UNb_2Al_{20} $(U)_{0.0435}(Nb)_{0.0870}(Al)_{0.8695}$	$G(UNb_2Al_{20},U:Nb:Al)-0.0435*{}^0H^{SER}_{U}-0.8695*{}^0H^{SER}Al-0.0870*{}^0H^{SER}Nb$ = **-19 455 +1.67*T** $+0.0435*G^{tetra}_{U}+0.8695*G^{fcc}_{Al}+0.0870*G^{bcc}_{Nb}$
$U_6Nb_4Al_{43}$ $(U)_{0.1132}(Nb)_{0.0755}(Al)_{0.8113}$	$G(U_6Nb_4Al_{43},U:Nb:Al)-0.1132*{}^0H^{SER}_{U}-0.8113*{}^0H^{SER}Al-0.0755*{}^0H^{SER}Nb$ = **-26 825 +3.65*T** $+0.1132*G^{tetra}_{U}+0.8113*G^{fcc}_{Al}+0.0755*G^{bcc}_{Nb}$

Table 11: Calculated invariant reactions and temperatures of the U-Nb-Al ternary system.

N°	T (K)	Reactions (cooling)
U_1	2152	liquid + $Nb_3Al \rightarrow \gamma(U,Nb) + Nb_2Al$
U_2	1598	liquid + $UAl_2 \rightarrow NbAl_3 + UAl_3$
U_3	1513	liquid + $NbAl_3 \rightarrow Nb_2Al + UAl_2$
E_1	1447	liquid $\rightarrow \gamma(U,Nb) + Nb_2Al + UAl_2$
P_1	1260	liquid + $NbAl_3 + UAl_3 \rightarrow \varphi_1:U_6Nb_4Al_{43}$
P_2	1200	liquid + $NbAl_3 + \varphi_1:U_6Nb_4Al_{43} \rightarrow \varphi_2:UNb_2Al_{20}$
U_4	1109	liquid + $\varphi_1:U_6Nb_4Al_{43} \rightarrow UAl_3 + \varphi_2:UNb_2Al_{20}$
U_5	1003	liquid + $UAl_3 \rightarrow UAl_4 + \varphi_2:UNb_2Al_{20}$
U_6	934	liquid + $NbAl_3 \rightarrow Al + \varphi_2:UNb_2Al_{20}$
U_7	914	$Al + UAl_4 \rightarrow$ liquid + $\varphi_2:UNb_2Al_{20}$

Titre:

The U-Nb-Al ternary system: experimental and simulated investigations of the phase equilibria and study of the crystal structure and electronic properties of the intermediate phases.

Auteurs:

Chantal Moussa[1], Alexandre Berche[1], Mathieu Pasturel[1], José Barbosa[1], Bertrand Stepnik[2], Sylvie Dubois[3] and Olivier Tougait[1,4]

Affiliation:

[1]*Institut des Sciences Chimiques de Rennes, UMR CNRS 6226, Université Rennes 1, Campus de Beaulieu, 35042 Rennes Cedex, France*

2 *AREVA/CERCA, 10 Rue Juliette Récamier, 69006 Lyon – France*

3 CEA/DEN/DEC, Cadarache, 13108 St. Paul Lez Durance, France.

[4]*Unité de Catalyse et de Chimie du Solide, UMR CNRS 8181, Université de Lille, 59695 Villeneuve d'Ascq, France*

Corresponding author : Olivier TOUGAIT, Unité de Catalyse et de Chimie du Solide, UMR CNRS 8181, Université de Lille, 59695 Villeneuve d'Ascq, France.

Email : tougait@univ-rennes1.fr

FIGURES

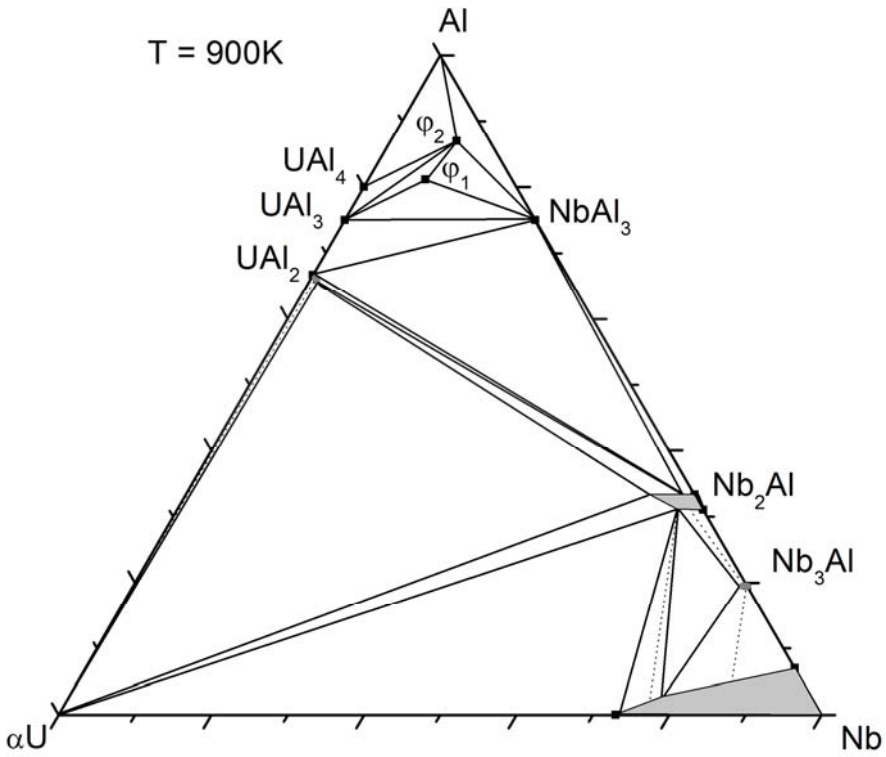

Figure 1: Experimental isothermal section at 900 K of the U-Nb-Al ternary system. The black solid lines delimit the three-phase fields. The thin dotted lines represent the tie-lines. The grey areas correspond to the homogeneity domains of the unary and binary phases. The symbols φ_1 and φ_2 stand for $U_6Nb_4Al_{43}$ and UNb_2Al_{20} respectively.

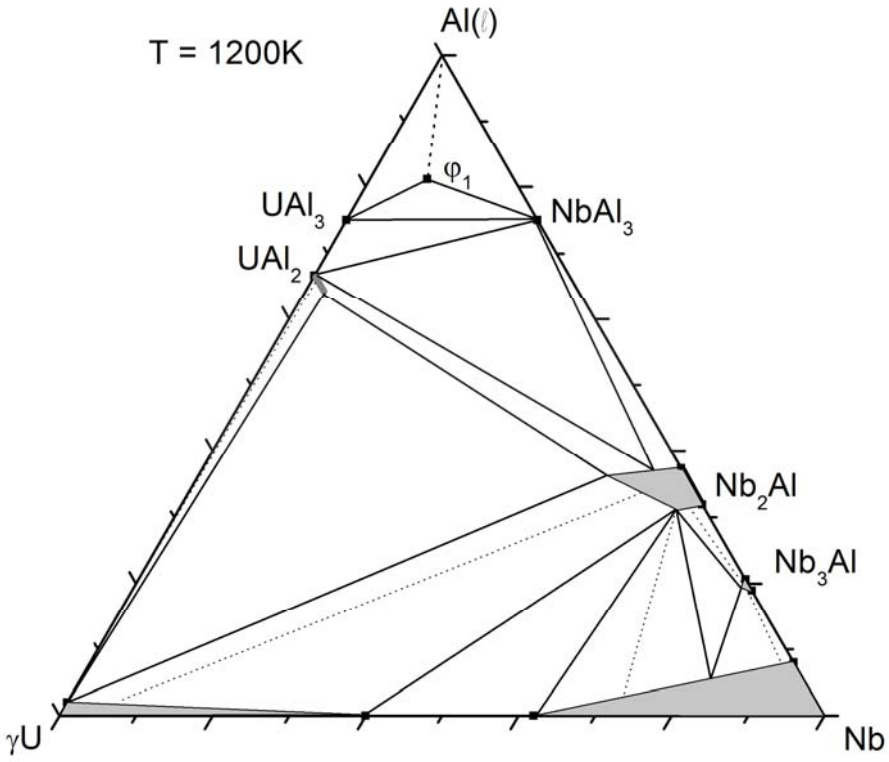

Figure 2: Experimental isothermal section at 1200 K of the U-Nb-Al ternary system. The black solid lines delimit the three-phase fields. The thin dotted lines represent the tie-lines. The grey areas correspond to the homogeneity domains of the unary and binary phases. The thick dotted line stands for the equilibrium with the liquid phase which was not determined. The symbol φ_1 stands for $U_6Nb_4Al_{43}$.

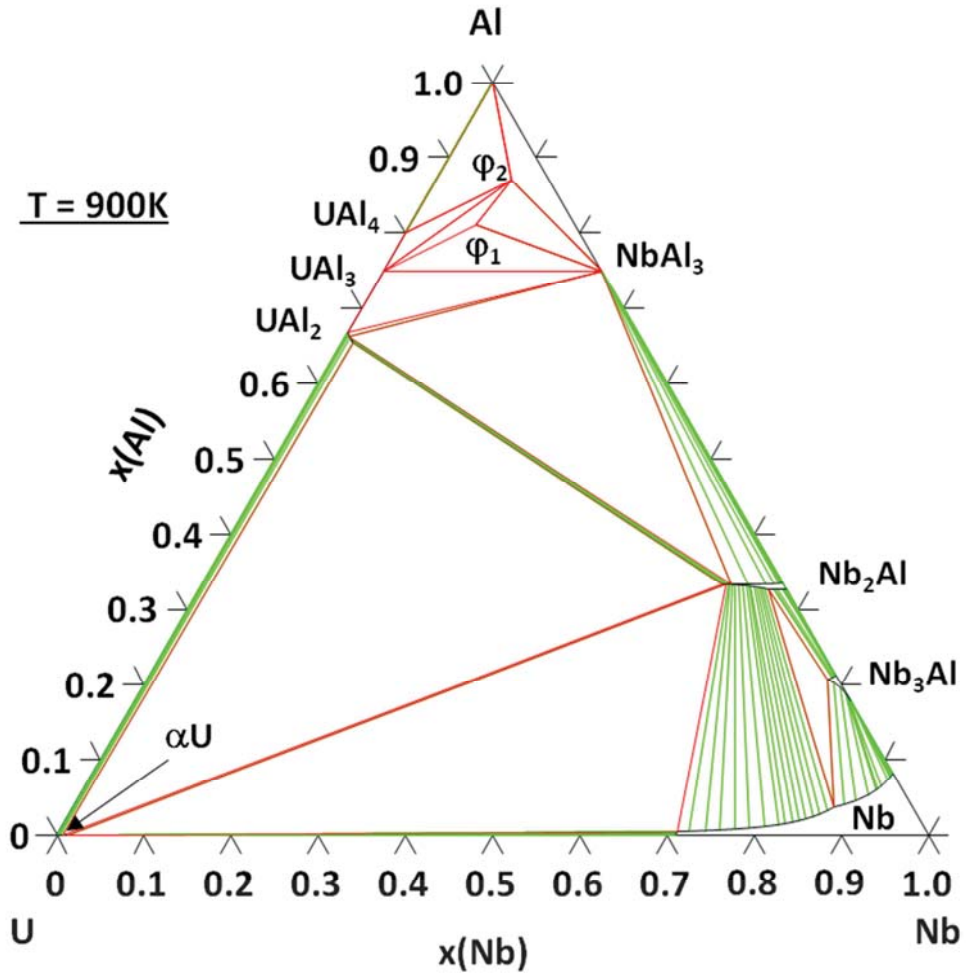

Figure 3: Calculated isothermal section at 900 K of the U-Nb-Al ternary system. The red solid lines stand for the equilibrium lines delimiting the three-phase fields. The green lines represent the tie-lines.

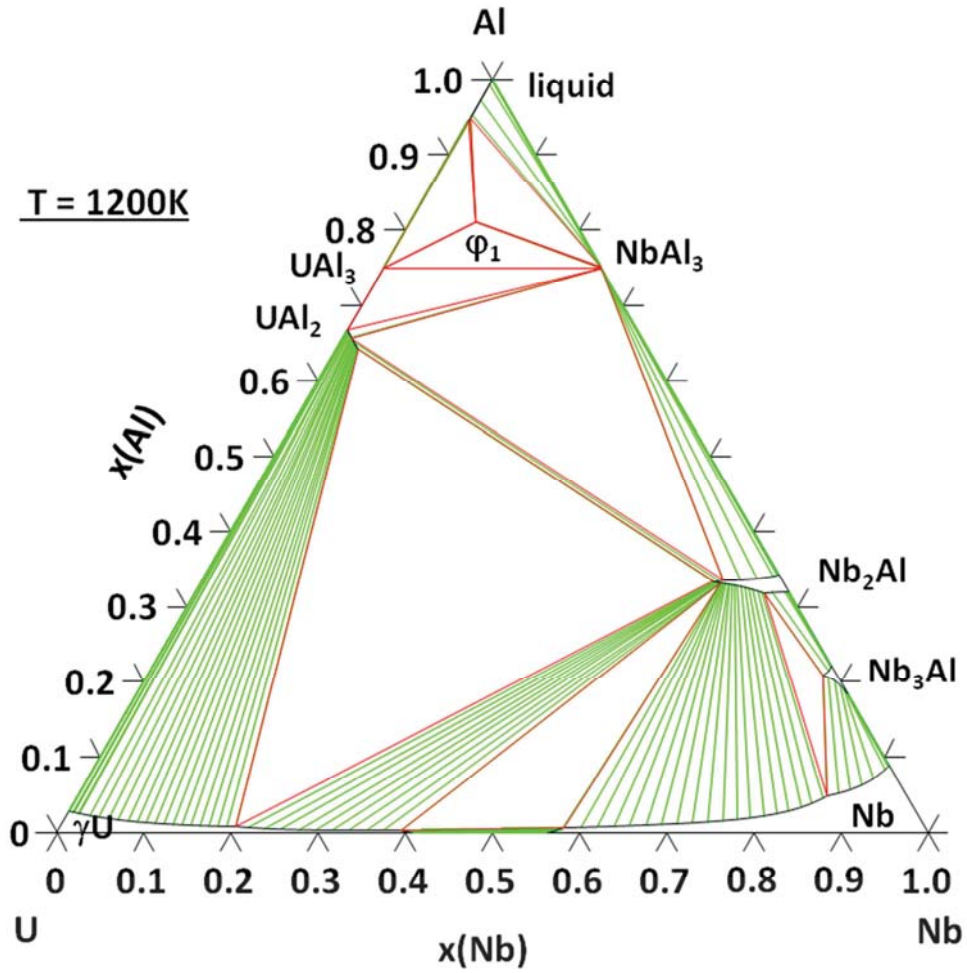

Figure 4 Calculated isothermal section at 1200K of the U-Nb-Al ternary system. The red solid lines stand for the equilibrium lines delimiting the three-phase field. The green lines represent the tie-lines.

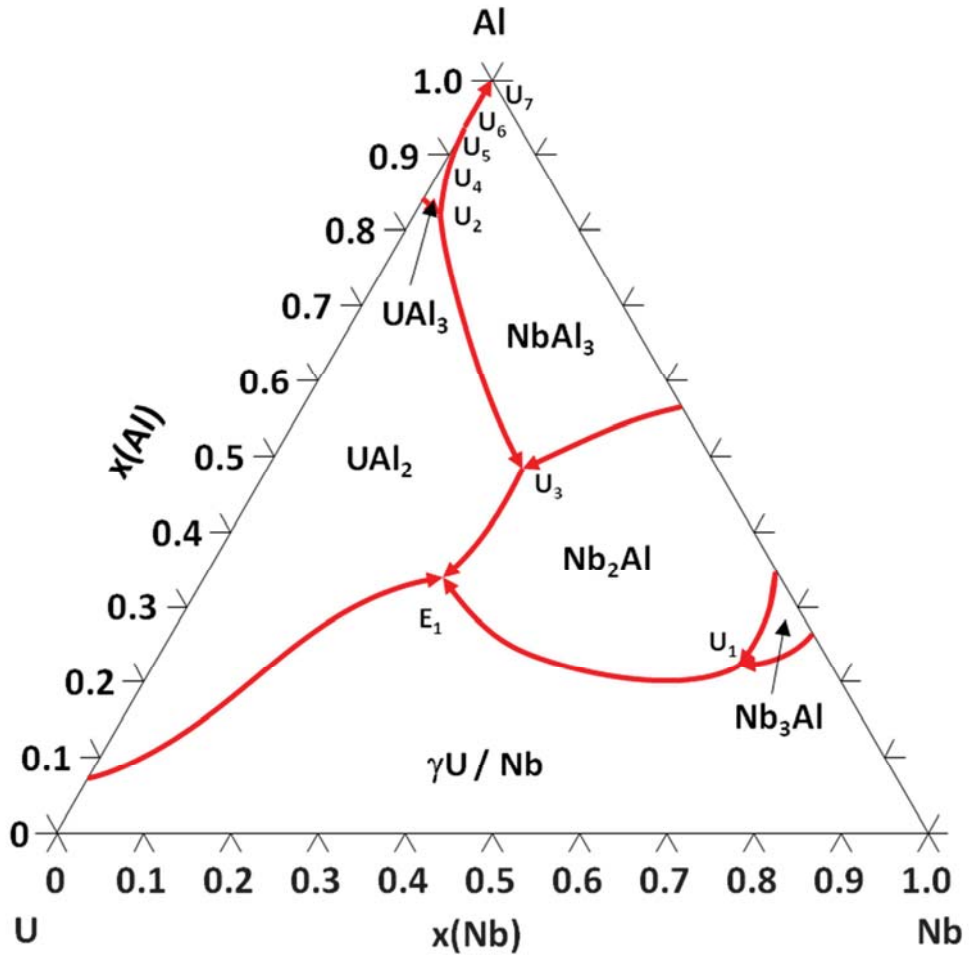

Figure 5 Calculated liquidus projection of the U-Nb-Al ternary system. The red solid lines correspond to the liquid paths.

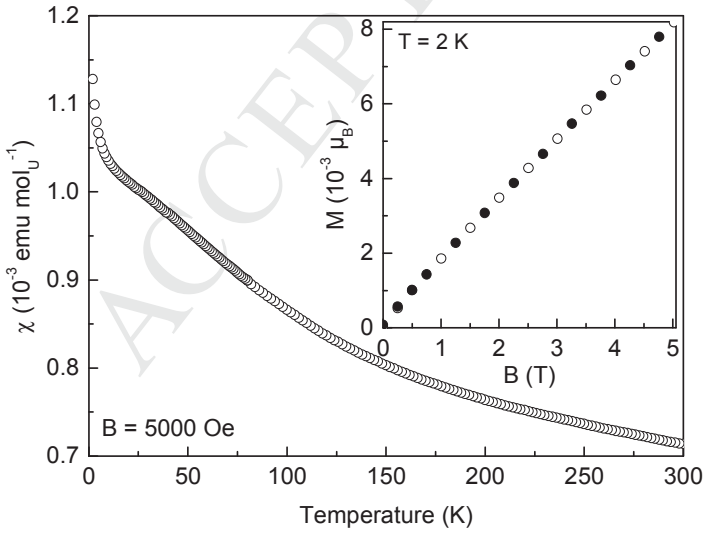

Figure 6: Thermal dependence of UNb_2Al_{20} magnetic susceptibility. The inset plots the magnetic field dependence of the magnetization isotherm at T = 2 K.

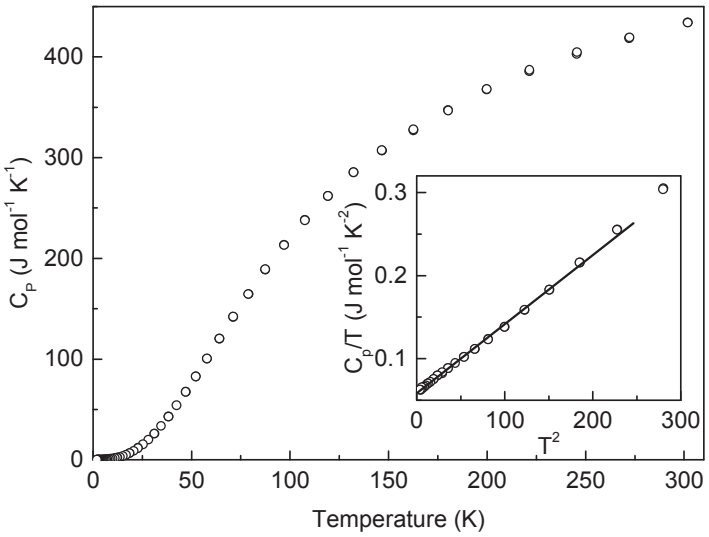

Figure 7: Thermal dependence of the UNb_2Al_{20} specific heat. The inset shows the low temperature domain of $C_P/T = f(T^2)$.

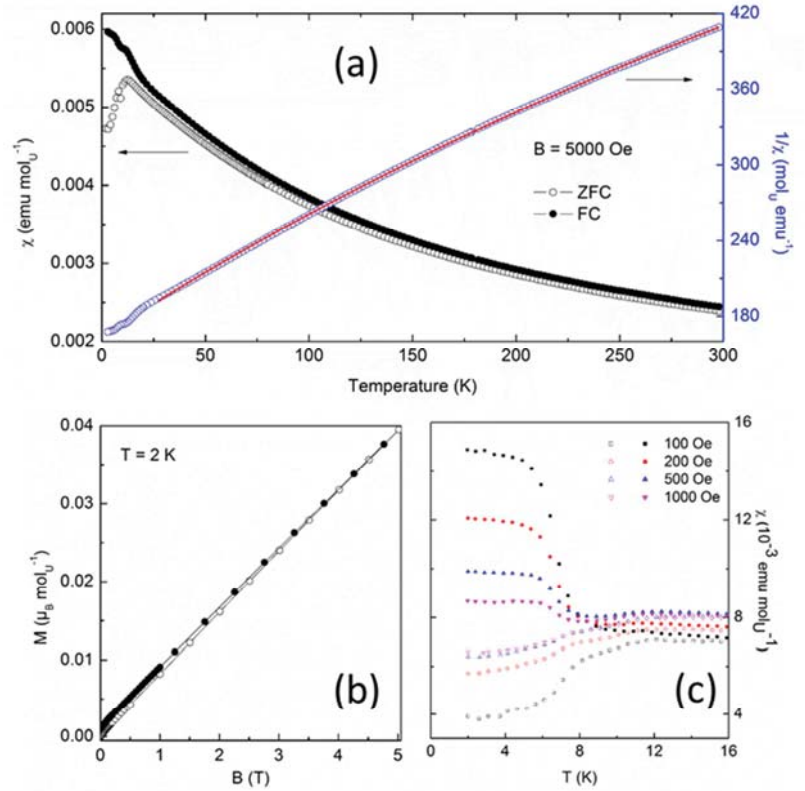

Figure 8 (a) Thermal dependence of $U_6Nb_4Al_{43}$ magnetic susceptibility (left) and its inverse (right) measured in the ZFC (open) and FC (full symbols) modes. The red line corresponds to the modified Curie-Weiss fit to $\chi^{-1}(T)$. (b) Magnetic field dependence of $U_6Nb_4Al_{43}$ magnetization isotherm measured at 2 K upon increasing (open) and decreasing (full symbols) magnetic field. (c) Low temperature part of $\chi(T)$ curves measured in the ZFC (open) and Fc (full symbols) under various applied magnetic fields.

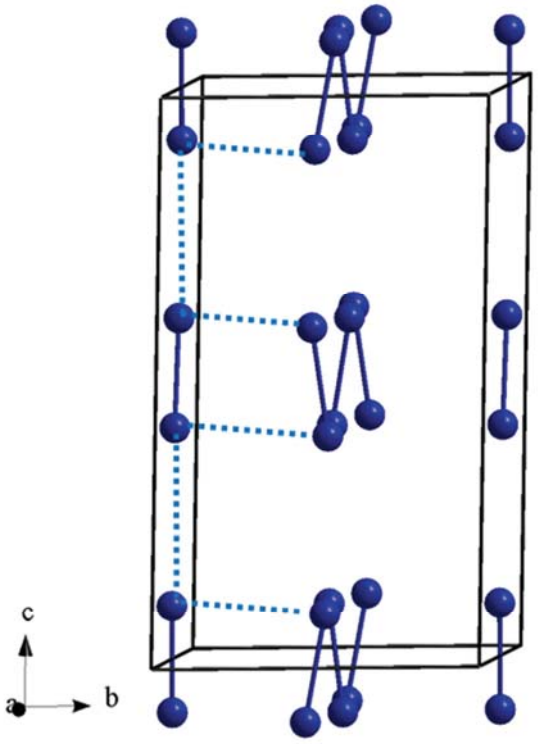

Figure 9: U-atom lattice in the $U_6Nb_4Al_{43}$ unit cell showing the formation of U-U dimers (solid lines) and the U spacing of 5.55(1) Å (dotted lines) for inter and intra chains.

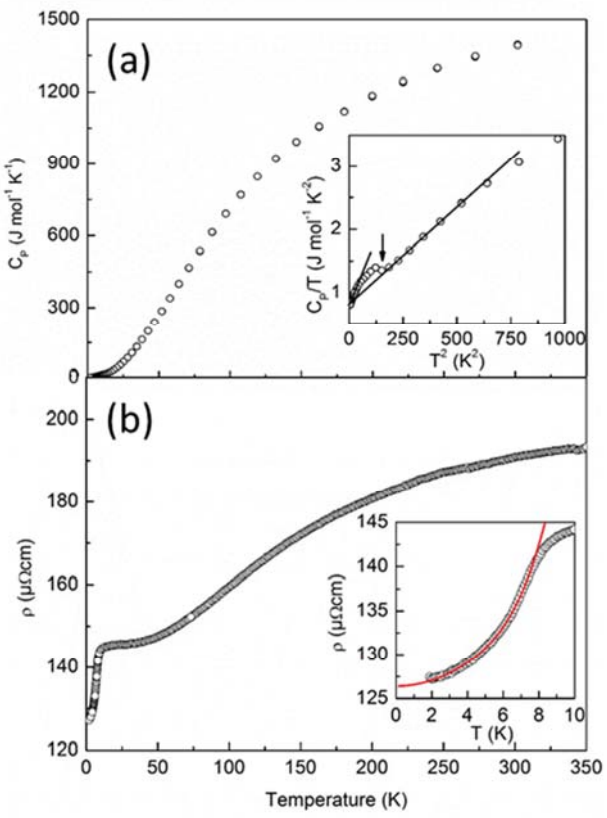

Figure 10: Thermal dependence of $U_6Nb_4Al_{43}$ (a) heat capacity and (b) electrical resistivity. The inset to panel (a) plots the T^2 dependence of C_p/T. The insets to panel (b) shows the fit of the experimental data according to Eq (IV).

Titre:

The U-Nb-Al ternary system: experimental and simulated investigations of the phase equilibria and study of the crystal structure and electronic properties of the intermediate phases.

Auteurs:

Chantal Moussa, Alexandre Berche, Mathieu Pasturel, José Barbosa, Bertrand Stepnik, Sylvie Dubois and Olivier Tougait

Highlights :

- Isothermal sections of the U-Nb-Al system were investigated for 900 K and 1200 K.
- The formation reaction of the intermediate phases was determined.
- The crystallographic properties of the equilibrium phases were checked.
- The thermodynamic properties was modelized by CALPHAD method.
- The electronic properties of the intermediate phases were investigated.